Investigation of solid-solid interface structure using a novel X-ray diffraction method

Thesis submitted in partial fulfillment of the requirements for the degree
"Doctor of Philosophy"

By
Mukhles Sowwan

Submitted for the senate of the Hebrew University
November 2002

This work was carried out under the supervision of
Prof. Yizhak Yacoby

Acknowledgments:

I am sincerely grateful to my supervisor Prof. Yizhak Yacoby for his kindness,

supervision, help and great support.

To Noam Sicaron , Yacov Girshberg, Marcel Brettschneider and Shuli Gilboa for

their help and support.

To Prof. Roy Clark, Prof Edwared Stern, Prof.Ron Pindak for their collaboration.

I am also grateful to the teams of MHATT-CAT and PNC-CAT beam lines at the

APS especially Eric Dufresne and Julie Cross for their help and support.

I dedicate this work to my mother scout for her support and help through all the way.

Abstract

We used a novel X-ray diffraction method COBRA (COherent Bragg Rod Analysis) developed in our laboratory, to investigate the atomic structure of solid-solid interfaces, specifically, Gd_2O_3 thin film epitaxially grown on a (100) GaAs substrate. The film structure is cubic and single domain with the [1 1 0] axis of the Gd_2O_3 perpendicular to the surface and its [-1 1 0] and [0 0 1] axes parallel to the GaAs [0 1 1] and [0 -1 1] axes, respectively. The Gd_2O_3 has a dielectric constant of approximately 10, with low leakage current densities of about 10^{-9}-10^{-10} Amperes/cm^2 at zero bias. Consequently Gd_2O_3 is an effective dielectric layer for the passivation of GaAs which opens very exciting possibilities for semiconductor devices.

Using COBRA we determined both the amplitude and phase of the complex x-ray scattering factors of the system under investigation. The information was obtained from the diffraction intensity measurements along the substrate defined Bragg rods. The system electron density and the atomic structure were obtained by Fourier transforming the complex scattering factors into real space.

The results showed that the stacking order of the Gd_2O_3 film layers is different from that of cubic bulk Gd_2O_3 and resembles the stacking order of Ga and As layers. Furthermore, in the first few Gd_2O_3 layers, Gd atoms were displaced to positions right above the Ga and As positions in the substrate and they relax towards bulk Gd_2O_3 positions with growing distance from the substrate.

TABLE OF CONTANTS

LIST OF FIGURES

Figure

CHAPTER I

INTRODUCTION

1.1 Solid-Solid Interfaces

Many electronic and electro- optic devices depend for their performance on interfaces between two materials one of which is a crystal while the other can be either a crystal epitaxially grown on it or an amorphous material. Such systems have full or partial two dimensional periodicity.

The phenomena that take place at the interface between the two materials are essential to the device performance. The best known example is the Si-SiO$_2$ interface. Field effect transistors are the most important elements of large –scale integrated circuits. They are used in all electronic devices, including computers. The Transistor action of modern field effect transistors takes place close to the interface between the Si crystal and its amorphous oxide. The oxide layers are getting progressively smaller. At present the oxides are a few tens of Angstroms thick while in future generation transistors the oxide layer thickness is expected to be as small as 15 angstroms. At these dimensions quantum effects and in particular tunneling start taking place. As a result the oxide is no longer a good barrier between the gate and the inversion layer. To overcome this difficulty researchers are looking now for alternative passivation layers to replace SiO$_2$. In these systems the quality of the interface between the Si crystal and the passivation layer is of crucial importance. It affects the electronic mobility, the dielectric strength and the long term reliability of the transistor. There are very many devices, including light emitting diodes, diode lasers, multi-layer capacitors, piezoelectric devices, super-conducting devices which contain one or more interfaces between a crystal and another amorphous or crystalline material.

Consequently, there is a large ongoing effort to investigate such material structures; to develop new ways to process them; to control their quality and to develop new devices based on them. In fact, many industrial and academic laboratories are equipped with systems for Molecular-Beam-Epitaxy (MBE) and Chemical Vapor Deposition that are used to prepare and manufacture such systems. Processing such material systems, developing new processing methods and new devices call for an intimate knowledge of the atomic structure of the materials in the vicinity of the interfaces.

  Many methods have been used to study the interface structures including:

1) High resolution transmition electron microscopy[1-5] (HRTEM):

In this method a nearly parallel electron beam travels through the sample and the direct (transmitted) beam and the diffracted beams are allowed to interfere with each other to form a "lattice" image. The resulting image reflects the periodicity of the crystal lattice since the lattice acts essentially as a phase grating. However, image interpretation can be complicated by inversions of contrast, which depend on the specimen thickness, objective lens defocus and additional interference effects.

2) X-Ray Reflectivity[8-13] (XRR):

X-ray reflectivity is now a common tool for investigating density profiles of thin films and multilayers in a nondestructive manner. In XRR, the change in reflectivity of a well collimated , monochromatic X-ray beam is monitored as a function of angle incidence, the incident and exit angle are kept identical (specular scattering). To obtain the required profile, models for the specular reflectivity are calculated and compared with experimental results. Inevitably, this leads to some uncertainty concerning the uniqueness of the model chosen.

3) Medium Energy Ion Scattering[14-17](MEIS):

MEIS has been used to examine the interfacial structure, strain and growth behavior of thin gate oxide films. MEIS is a lower energy version of Rutherford backscattering in which a high energy and angular resolution detector is used to obtain detailed information about atomic structure and composition in the top 50-200Å of the sample. The physics of back scattering is well understood and a depth profile of elemental constituents in the sample can be calculated from the MEIS data. Unfortunately, MEIS analysis of a single sample may require ~10 h to get reasonable statistics. Because protons are used as probes in MEIS, elements heavier than hydrogen can be characterized in the sample. Therefore, one can determine the position and concentration of nitrogen in very thin oxide/nitride (or more complex) stacks using MEIS.

4) X-ray Absorption Fine Structure [18-22](XAFS):

XAFS spectroscopy is usually divided into two spectral regions: X-ray absorption near edge structure (XANES) and extended x-ray absorption fine structure (EXAFS). XANES covers the range from about 10 eV below the main edge up to 50 eV above it, whereas EXAFS covers the rang from about 30 eV to about 1500 eV above the edge. Both EXAFS and XANES are strongly affected by the structure. However XANES is strongly affected by the chemistry of the material and the valence of the probe atom. Unfortunately the full chemical and structural information in XANES is rather difficult to obtain because the spectrum requires calculating a stronger interaction between the excited photoelectron and the surroundings than does EXAFS. The analysis of both XANES and EXAFS measurements is particularly difficult when the probe atom is present in more than one inequivalent site. In this case the structure obtained is an average of the structures surrounding all probe atoms of the same

species. This problem is particularly severe in films and interfaces where the structure may change from one monolayer to the next but the atoms involved are the same.

5) X-Ray holography[23-28] :

In this technique, atoms within the sample stimulated with an external source such as x rays or high-energy electrons, or nuclei undergoing radioactive decay, can emit radiation, which can reach the detector directly (the reference wave) or after scattering off the electrons of nearby atoms (the object wave). The pattern of interference between the direct and scattered radiation can be mapped out by varying the angular position of the detector. This pattern can be viewed as a hologram from which a real-space image can be reconstructed numerically. Holography doesn't really record the phase of the object wave with respect to the reference wave, but only the cosine of the phase difference. A twofold sign ambiguity therefore remains. As a result, in the reconstruction of a 3D image from the hologram, one gets not only the real image but also a twin image that's inverted about the reference point (here, the fluorescing atom). The superposed images can be out of phase with each other, which can lead to cancellations, distortions, and problems with atom identification. Here again the structure is an average over the structure surrounding atoms of the same species located at inequivalent sites.

6) X-ray standing waves[29-31] (XSW):

The X-ray standing wave (XSW) technique, inherently an interferometric method, employs the interference field, which is produced by the superposition of an incoming plane and coherently scattered waves, as a probe to measure distances of the order of subangestrom.

The advent of the Synchrotron X-ray Radiation (SXR) sources has had a major impact on the XSW technique. High X-ray intensities cut down on measuring times, rending

the study of surfaces possible which otherwise would have been prohibited because of contamination problems in the course of prolonged measuring times. Next generation SXR sources may initiate another quantum leap forward. The brilliance of these sources, and brilliance is the real figure of the merit of XSW experiments, is supposed to increase by several orders of magnitude compared to present-day sources.

7) Diffuse X-ray scattering[32-35](DXRS):

A number of X-ray diffuse scattering studies have already been carried out on multilayers of amorphous materials, polymers, rare earths, and crystalline semiconductors using conventional x-ray nonspecular reflectivity techniques, where the momentum transfer is kept within the scattering plane of the specular reflected beam. In this case the intensity is mediated by the Fresnel transmission function, giving rise to the so-called "Yoneda wings". Also, the achievable momentum range is considerably diminished by the constraint of this rocking scan, where θ can neither be smaller than zero nor grater than 2θ, the angle between incident and scattered waves. Using this technique one obtains only a statistical average over large ensembles but with high strain sensitivity.

8) Grazing-incidence x-ray diffraction [47,48]:

Grazing-incidence x-ray diffraction is a scattering geometry combining the Bragg condition with the conditions for x-ray total external reflection from crystal surfaces. It is commonly nowadays recognized that grazing incidence x-ray diffraction (GID) is superior to conventional x-ray diffraction techniques in the study of the crystal structure of thin surface layers. GID has been successfully applied to studies of surface treatment, oxidation and ion implantation of semiconductor wafers and to the analysis of strain relaxation in epitaxial layers and multilayers. The high brightness of third generation x-ray synchrotron sources provides an opportunity to perform high-

resolution measurements in GID by analogy with high resolution diffractometry and reciprocal space mapping in the conventional Bragg case.

9) X-ray mapping of reciprocal space [48,49] :

Reciprocal space mapping (RSM) is a promising technique for the study of orientational and twinning effects in heteroepitaxial structures. RSM is realized by adding a Ge crystal (the analyzer) between the sample and the detector to select the diffracted beam over a small angular rang. Reciproical space maps are useful for studying less perfect structures because they enable a separation of the effects of the lattice strain variations, curvature, and lattice orientations on the reciprocal space peak broadening.

Generally, all these techniques provide important information on the system under investigation. In particular some of them XAFS and x-ray holography provide information on neighbor correlations but they all suffer from one or both of the following limitations:

a) Obtaining reliable structural information requires a correct structural model; in other words one needs to guess a model and then refine its parameters, Due to the complexity of such system it is often difficult to guess the correct model.

b) The information obtained provides only the average structure about probes located at inequivalent positions in the system.

The COBRA technique[36-38] developed by *Yacoby et al.* overcomes these limitations because it is model independent, provides direct structural information on the system under investigation, utilizing the high- brightness characteristics of 3rd generation synchrotron radiation.

Most importantly, we determine both the amplitude and phase of the complex structure factor of the system under investigation by measuring the diffraction

intensities along the substrate-defined Bragg-rods and hence obtain the three-dimensional electron density distribution by back Fourier transformation.

1.2 The Gd$_2$O$_3$-GaAs Interface:

There have been many attempts over the past 30 years to find an insulating layer that will passivate the (100) GaAs surface. Most of the attempts have failed either because the interfacial state density was unacceptably high, leading to significant leakage current, or because the layers were not thermodynamically stable relative to the GaAs interface. A promising direction was initiated by Hong et al.[41] in their studies of (Ga$_2$O$_3$)$_{1-x}$/(Gd$_2$O$_3$)$_x$ -GaAs interfaces. In this work these authors showed that while pure Ga$_2$O$_3$ does not passivate GaAs, the mixed oxide is electrically insulating with high electrical breakdown strength if x>14%. These results pointed the way to Gd$_2$O$_3$ as an effective dielectric layer for the passivation of GaAs. Subsequent studies confirmed that Gd$_2$O$_3$ is indeed potentially useful as a passivation layer exhibiting a mid-gap interfacial state density of as little as 10^{11} cm^{-2} eV^{-1}, only slightly higher than that of Si-SiO$_2$ interfaces. With a dielectric constant of ~10, this oxide is an excellent dielectric with leakage current densities in the range ~10^{-9} - 10^{-10} A/cm^2, showing much promise as a passivation layer. Gd$_2$O$_3$ films are also viewed as potential high dielectric constant passivation layers for Si. However, the reason for such a remarkably low interfacial state density is not understood at this time.

Kortan et al.[42] found that films grown under conditions similar to the growth conditions of our sample grow as a single cubic crystal. The Gd$_2$O$_3$ <110> axis is perpendicular to the (100) GaAs substrate surface, the <001> Gd$_2$O$_3$ axis coinciding with the <011> GaAs axis and the orthogonal <1-10> Gd$_2$O$_3$ axis coinciding with the <0-11> GaAs axis. In principle the Gd$_2$O$_3$ may have two orientations rotated 90

degrees relative to each other, however the Kortan et al. experiments show that the film grows as a single domain; what determines the specific orientation is not clear.

XAFS measurements have shown that the Gd oxygen bonds increase by 2.7%+/- 0.6% and this increase is consistent with the increase in the lattice spacing perpendicular to the interface.

While the studies of Koratn et al. and others clarifying the crystal type and its orientation relative to the GaAs subatrate, they did not determine the detailed atomic structure of the Gd_2O_3 film.

In this work we studied the atomic structure of Gd_2O_3 thin film epitaxilly grown on a (100) GaAs substrate. We obtained the atomic structure of this system using the COherent Bragg Rod Analysis (COBRA) method, which is especially sensitive to the arrangement of atoms in epitaxial films and interfaces. The results obtained provide very detailed and quite surprising new information on the structure of the Gd_2O_3-GaAs system.

1.3 Outline

The outline of this dissertation is as follows. In chapter II, the COBRA method, the main system requirements , the experimental setup , the determination of the complex scattering factors from the experimental data and the determination of the electron density function from the calculated scattering factors by Fourier transformation are explained.

In chapter III, the sample preparation, the sample properties and the experimental results are presented, the Gd_2O_3 film was epitaxially grown on GaAs substrate at Bell labs, USA. The experiments were performed at the advanced photon source at Argone National Labs, Chicago, USA. We measured the diffraction intensities along 12 symmetry inequivalent Bragg rods, h 1 -1, h 0 0,h 1 1, h 0 -2, h 2 0, h 2 -2, h -2 -2, h 3 1, h 3 -1, h-1-3,h -3 -3 and h 3-3, in addition to h-1 1.

In chapter IV, the data analysis is presented, the analysis starts with building a model for the Gd_2O_3-GaAs interface to consider as a reference structure, then the complex scattering factors are determined using the COBRA method from the experimentally measured diffraction intensities. The quality of the agreement between the calculated and experimental diffraction intensities constitutes a measure of the quality of the electron density obtained.

In chapter V, the results are discussed, and chapter VI contains the conclusions of the research.

CHAPTER II

METHODOLOGY

2.1 The Periodicity of Epitaxial Films

Epitaxially grown thin films are either fully or partially periodic in two dimensions and are a-periodic in the third dimension. In this study we will consider 3 types:

1. Full 2D periodicity with a film period equal to the substrate period:

    In this case the dimensions of the film unit cell equals that of the underlying substrate, for example GaAs\ AlAs heterostructures and $BaTiO_3$ thin film epitaxially grown on $SrTiO_3$ substrate.

2. 2D Periodicity with a film period not equal to the substrate period but still commensurate with it, for example Gd_2O_3 thin film epitaxially grown on GaAs substrate crystal.

3. Partial Two Dimensional Periodicity:

Previous studies by Takahashi et al.[43,44] on Si-SiO_2 have found SiO_2 crystallites distributed in the amorphous oxide film; the crystallites were grown as small columnar single crystals stemming from the interface as a coherent two dimensional epitaxial array. According to their studies, the probability of finding the crystallites decays almost exponentially as a function of the distance from the interface. Therefore, it is concluded that the crystallites are dense at the interface forming partial two dimensional periodic structures.

2.2 X-ray Diffraction from Systems with 2D Periodicity

In general, since the substrate is periodic in 2D and the epitaxial film is chemically bonded to it, the scattering factors along the substrate defined Bragg rods have the form of 2D delta functions. To calculate these scattering factors we divide the system into substrate defined unit cells and the electron density of such systems can be expressed as $r(x, \vec{R}_{i,j} + \vec{r})$, where x is the coordinate perpendicular to the interface, $\vec{R}_{i,j}$ is the in-plane position of the (i, j) unit cell and $\vec{r}$ is the in-plane position within the unit cell. In general r varies with (i, j). The complex scattering factor $T_{h,x}(x)$ along the (h,x) Bragg rod is proportional to the Fourier transform of the electron density:

$$T_{h,x}(k) = \int_V d^2 r dx \sum_{i,j} r(x, \vec{R}_{i,j} + \vec{r}) \exp\{i[(\vec{R}_{i,j} + \vec{r})\vec{k}_{h,x} + kx]\} \qquad (2.1)$$

Since $\vec{k}_{h,x}$ is a Bragg rod vector, $\vec{R}_{i,j}\vec{k}_{h,x} = 2pn$. Thus, Eq 2.1 reduces to the form:

$$T_{h,x}(k) = \int_V d^2 r dx \exp\{i[\vec{r}\vec{k}_{h,x} + kx]\} \sum_{i,j} r(x, \vec{R}_{i,j} + \vec{r}) \qquad (2.2)$$

Namely, the scattering factor along the Bragg rods is the Fourier transform of $\sum_{i,j} r(x, \vec{R}_{i,j} + \vec{r})$. We shall refer to this as the electron density of the *folded system* and it is obtained by moving all atoms into one 2D substrate defined unit cell using 2D unit cell vectors (fig 2.1 explains the concept of folding).
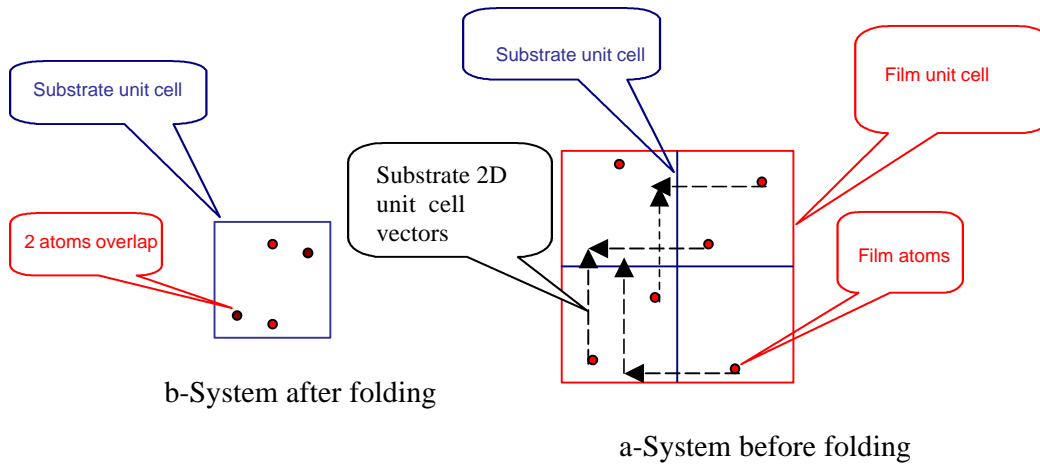
Fig2.1 schematic representation of the folding procedure using substrate 2D unit cell vectors. a- System before folding, red square represents film unit cell, red circles represent film atoms, blue squares represent substrate unit cells. b- System after folding, blue square represent substrate unit cell.

Now let us consider the X-ray diffraction from systems with full and partial 2D periodicity:

1- Systems with Full 2D periodicity with a film period equal to the substrate period:

In this case the folded structure is obtained by folding the atoms of one film unit cell into one substrate unit cell." atoms from different unit cells will overlap after folding".

Notice that in this case the complex scattering factor (CSF) along the Bragg rods contains all the information on the structure of this 2D periodic system .

2 . 2D periodic system with film period not equal to the substrate period but still commensurate with it:

In this case the folded structure is obtained by folding all the atoms of the composite cell into one substrate unit cell.

Notice that we only measure the diffraction intensity along the substrate defined Bragg rods, which do not contain all the information about the film and the interface, because a part of the information is contained in other Bragg Rods (the film Bragg rods). But the complex scattering factors along the substrate defined Bragg rods are still the Fourier transform of a well defined real space electron density, namely, the electron density of the folded system which contains all the information about the folded structure.

3. Systems with partial two dimensional periodicity:

In this case the folded structure is obtained by folding all the crystallites into one substrate unit cell .Notice that the presence of local incommensurability and strain will give rise to diffuse scattering throughout reciprocal space. Thus, important information about the film is contained in the diffuse scattering intensity function .But also in this case the complex scattering factors along the substrate defined Bragg rods are still the Fourier transform of a well defined real space electron density, namely, the electron density of the folded system which contains all the information about the folded structure.

2.3 Outline of the COBRA Method

The COBRA method is used to determine the complex scattering factors (CSFs) of two dimensional systems along the Bragg rods and the folded electron density by Fourier transforming them into real space.

The method consists of the following steps:

1- Measurement of the diffraction along the Bragg rods:

This is the Experimental part of the Method, The system requirements, the experimental setup and technique are explained in this section.

2- The structure determination

    a) Determination of the Complex Scattering Factors:

we determine both the amplitude and phase of the complex scattering factors of the system under investigation, using information obtained from the diffraction intensity measurements along the substrate defined Bragg rods.

   b) Obtaining the electron density:

The system electron density and the atomic structure are obtained by Fourier transforming the complex scattering factors into real space.

 c) Iteration and comparison with the experimental results

2.4   Measurement of the Diffraction along the Bragg Rods

2.4.1 The main system requirements:

To make the experiments practical, coherent X-ray beams with high intensity are needed. Third-generation synchrotron storage rings provide the x-ray beam qualities, flux and brilliance, that are needed for frontier experimentation. Flux and brilliance are benchmarks of x-ray beam quality. Both are based on a measure of the number of

photons per second in a narrow energy band-width and in a unit of solid angle in the horizontal and vertical directions. Flux is the number of photons per second passing through a defined area, and is the appropriate measure for experiments that use the entire, un-focused x-ray beam. Brilliance is a measure of the intensity and directionality of an x-ray beam. It determines the smallest spot onto which an x-ray beam can be focused.

The X-ray beams generated by undulators in 3rd generation synchrotrons have a high brilliance of the order of 10^{19} photons/(sec.mm^2.mrad^{2}0.1% bandwidth).The beam can be monochromatized to 0.01% bandwidth and collimated to a spatial divergence of 10ìrad. The longitudinal coherence length in this case is about 1ìm and the transverse one is about 10ìm.

2.4.2 The experimental setup:

The general scattering geometry from two dimensional crystals is shown in figure 2.2
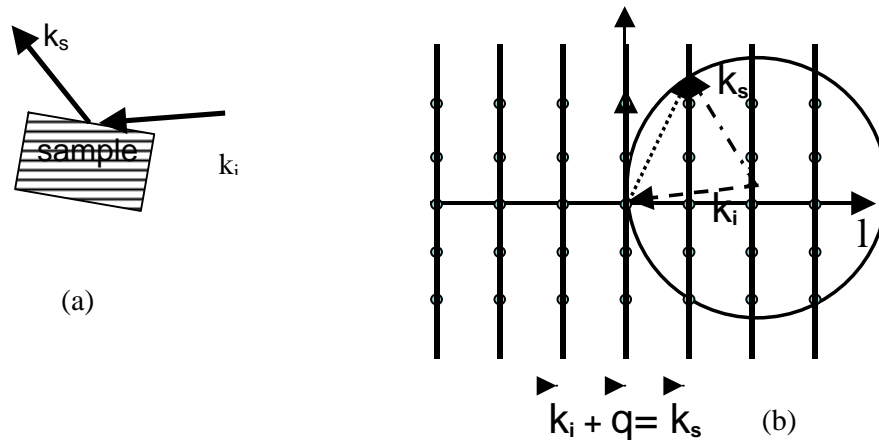
● Real Space   ● Reciprocal Space

(a)

$k_i + q = k_s$ (b)

Fig 2.2 a- Scattering geometry: The incident beam with a wave vector $\mathbf{k}_i$ impinges on the sample surface and the scattered beam with a wave vector $\mathbf{k}_s$ scattered from the sample. b- Reciprocal space representation of the scattering geometry: The dots represent the GaAs reciprocal lattice points.The vertical lines represent Bragg rods. The circle represents the Ewald sphere. The three arrows represent incident $\mathbf{k}_i$,the scattered
$\mathbf{k}_s$ and the crystal momentum transfer $\mathbf{q}$.

In real space the beam was incident on the sample with small incidence angle, but in contrast to GID we used angle that is larger than that of the total external reflection. $\mathbf{k_i}$ and $\mathbf{k_s}$ are the wave-vectors of the incident and the scattered beams respectively. The scattering from a 2-D crystalline material in reciprocal space extends in rods in the direction, perpendicular to the planes of the thin film monolayers. Bragg rod diffraction occurs when the scattering vector $\mathbf{q}$ ends on the (k,l) Bragg rod.

In fig 2.3 we can see the experimental setup used in the experiments. The sample was mounted at the center of a six circle goniometer and had 4 rotational degrees of freedom. The incident beam impinged on the sample surface and the diffracted beam was detected by a detector mounted on the detector arm that had two rotational degrees of freedom.

The measurement of the diffraction intensity along a Bragg rod is in principle achieved by rotating the sample around an axis perpendicular to its surface and by moving the detector to the position where the diffracted beam is expected to be.
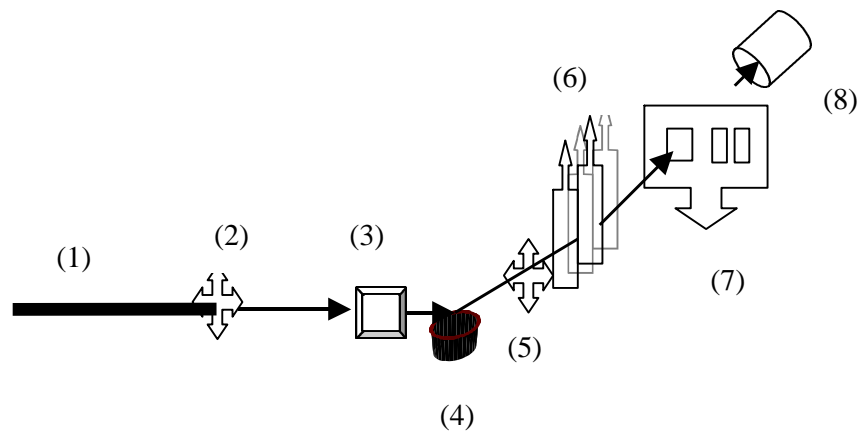

Fig 2.3 Experimental setup inside the hutch.

      1-Monochromatic incident x-ray beam.

      2-Input slit.

      3- Reference detector.

      4-Sample mounted at the center of a six circle goniometer.

      5- Output slit. (used during the alignment procedure).

      6- Automatic filter unit (Aluminum foils)

      7- Signal detector.

Measurement of the diffraction intensities along the Bragg rods requires precision in several ways. The scan must be made along the Bragg rod and not fall off to the sides. The relative intensities along the rod and among different rods must be quantitatively correct to within a few percent. The background associated with scattering processes not associated with the diffraction along the Bragg rods must be subtracted. To address these needs we have developed a new LABVIEW based software package that controls the entire experimental system including the goniometers used. The software system includes the geometry code and is capable of controlling both Huber and Kappa type 6 circle goniometers figs.2.4a and 2.4b. It fully replaces 'SPEC' and offers the user various advantages in the operation and the graphic display of the results.

Fig.2.4a. Kappa type six circle goniometer at the MAHHT CAT beam line at APS.
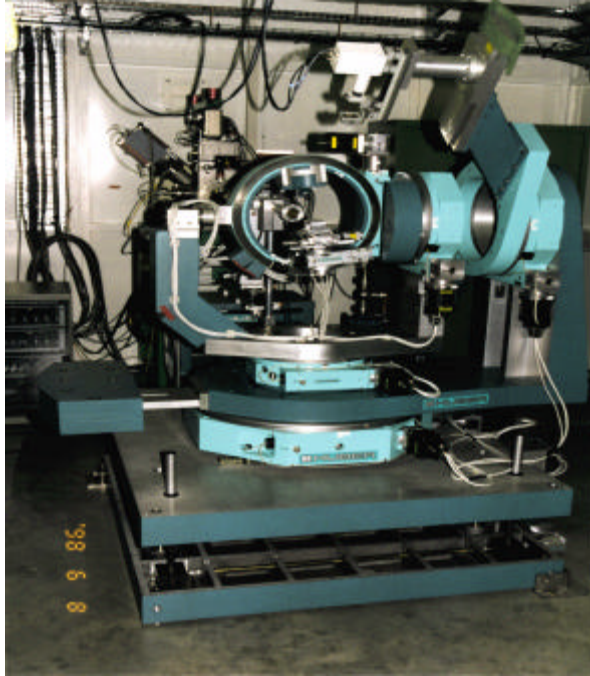
Fig 2.4b. Huber six circle goniometer .

To obtain reliable control of the goniometers we measured the orientation of the various rotation axes relative to each other. This was done using an autocollimator mounted on the detector arm and a mirror mounted at the sample position. Once the rotation axes are correctly determined the auto-collimator and the mirror must remain aligned with respect to each other under arbitrary rotations around an arbitrary axis. After determining the rotation axes vectors the misalignment between the autocollimator and the mirror did not exceed 400 μradians.

We used an incident beam with 10keV photon energy. This energy was chosen because it is, approximately, the largest energy that is still safely below the absorption edges of all the relevant constituents. Thus we did not need to worry about fluorescence. The incident beam was focused vertically to about 100 microns using K-B mirrors, slitted down horizontally to 0.5mm and its orientation relative to the

goniometer axes was determined to within 100µrad . Notice that with our software system the incident beam need not to be at any particular orientation relative to the goniometer. (see Fig 2.3 the experimental setup).

The sample was mounted on the goniometer in such a way that the goniometer center of rotation was on the sample surface and the incident beam impinged on the sample at this same point. We first found a number of Bragg reflections and used them to determine the orientation of the sample reciprocal unit cell. We found in all our experiments that any other Bragg point was within about 2mrad in the sample and detector orientations from the corresponding calculated values. This is not enough to guarantee accurate rod scans. We therefore carried out scans perpendicular to the rods at several points along each rod and use the corrections to make accurate rod scans. The corrections reduced the errors to less than 200 µrads which is small compared to the detector acceptance angle of 3 mrads. These errors also cause negligible inaccuracy in the position along the Bragg rods.

 The diffracted beam intensity was measured using a plastic scintillator photomultiplier detector unit followed by a stable dc preamplifier. The advantage of this unit in comparison to the ordinary photon counting detectors is its linearity up to intensities of several hundred thousand photons per second. We used an automatic calibrated filter unit to measure the intensities very close to the Bragg peaks see fig2.3. The incident intensity was measured by an ionization chamber located just before the sample. We took precautions to make sure that the entire incident beam measured by the reference detector contributed to the diffraction and the entire diffracted beam was measured by the signal detector. This requirement was difficult

to satisfy when the incidence angle was below 5 deg., namely in measurements along [h 0 0] Bragg rod for h<1.

Finally, the background was removed in the following way:

We installed in front of the signal detector a paddle (see Fig. 2.3) which had two types of openings: a 3x3mm^2 opening to let the signal through and a set of two 3x2mm^2 openings at a distance of 3mm from each other to stop the signal and let the background through. At each point along the Bragg rod a motor moved the paddle so that for half the integration time the signal went through and then the background was let through for the second half. The measurement was carried out at equal steps along the Bragg rod , with step size of 0.01 reciprocal unit cell units. The total scan time per Bragg rod was amounted to about 2 hours.

The diffracted beam intensity is proportional to the Fourier transform of the electron density. The proportionality constant depends on the experimental geometry and on the polarization of the incident beam. In all our measurements the axis perpendicular to the sample surface was kept in the plane defined by the incident X-ray beam and the experimental floor. Thus the incident beam was always polarized parallel to the sample surface. The proportionality constant in this case is given by:

(2.3)

$$ p = \frac{\sin^2(j)}{.\ (\ )\ .\ (\ )} + \frac{\cos^2(j)\sin(q^2)}{.\ (\ )} $$

Where j is the angle between the polarization vector and the component of the diffracted wave-vector on the sample surface and q_1 and q_2 are the angles

between the sample surface and the incident and diffracted beam wave-vectors, respectively.

In all subsequent displays the diffraction intensities were divided by this constant so that the displayed results are proportional to the Fourier transform of the electron density up to a factor that is independent of geometrical diffraction conditions.

2.5 The structure determination

2.5.1 Determination of the complex scattering factors (CSFs):

As I mentioned before the complex scattering factor (CSF) along the Bragg rods contains all the information on the structure of the 2D periodic system and the electron density can be obtained from it by Fourier transforming the CSF into real space. The diffraction along the Bragg rods is composed of several coherent contributions: scattering from the electron density of the ideal semi-infinite substrate crystal, scattering of the electron density of the film grown on it and scattering from the difference between the electron densities of the ideal semi-infinite crystal and the actual crystal, including any film-induced distortions. Note that the electron density of the semi-infinite ideal substrate crystal is known and therefore so is its CSF. In a more general sense the total scattering intensity can be considered as coherently composed of two contributions: the scattering of a known reference electron density and that of an unknown electron density such that the combination of the two yields the electron density of the real system. The reference part can be for example a simple model of the system.

At any two adjacent points along a Bragg rod differing by $\Delta\vec{k}$

$$S(\vec{k} - \frac{\Delta\vec{k}}{2}) + U(\vec{k} - \frac{\Delta\vec{k}}{2}) = T(\vec{k} - \frac{\Delta\vec{k}}{2})$$
$$S(\vec{k} + \frac{\Delta\vec{k}}{2}) + U(\vec{k} + \frac{\Delta\vec{k}}{2}) = T(\vec{k} + \frac{\Delta\vec{k}}{2})$$

(2.4)

Where, S, U and T are the complex scattering factors due to the reference, unknown and total electron densities, respectively.

We now make use of the fact that the complex scattering factors vary continuously along the Bragg rods and make the approximation that at two adjacent points along a Bragg rod:

$$U(\vec{k} - \frac{\Delta k}{2}) \cong U(\vec{k} + \frac{\Delta\vec{k}}{2}) = U_a(k).$$

(2.5)

Taking the absolute value of Eq. 2.4yields:

$$\left| S(\vec{k} - \frac{\Delta\vec{k}}{2}) + U_a(\vec{k}) \right| = \left| T(\vec{k} - \frac{\Delta\vec{k}}{2}) \right|$$
$$\left| S(\vec{k} + \frac{\Delta\vec{k}}{2}) + U_a(\vec{k}) \right| = \left| T(\vec{k} + \frac{\Delta\vec{k}}{2}) \right|.$$

(2.6)

In Eqn.2.6 the absolute values of the total scattering factors are proportional to the square root of the intensity. This yields two real equations that can be solved for one complex unknown. For clarity a graphical representation of these equations is shown in Fig2.5. The figure on the left represents the equations at $\vec{k} - \frac{\Delta\vec{k}}{2}$ and $\vec{k} + \frac{\Delta\vec{k}}{2}$. The corresponding complex numbers are marked with indices 1 and 2, respectively.

The figure on the right represents the equations with $\vec{k} + \dfrac{\Delta\vec{k}}{2}$ and $\vec{k} + \dfrac{3\Delta\vec{k}}{2}$ and the corresponding indices are 2 and 3 respectively. Each pair of equations has two solutions U_a and U_b shown as solid and dashed lines, respectively. Under the assumption that U varies slowly along the Bragg rods the correct pair of solutions are the ones that change the least when going from one point to the next; namely U_{1a} and U_{2a}. This procedure then provides the unknown complex scattering factors and the complex total scattering factors along each Bragg rod.
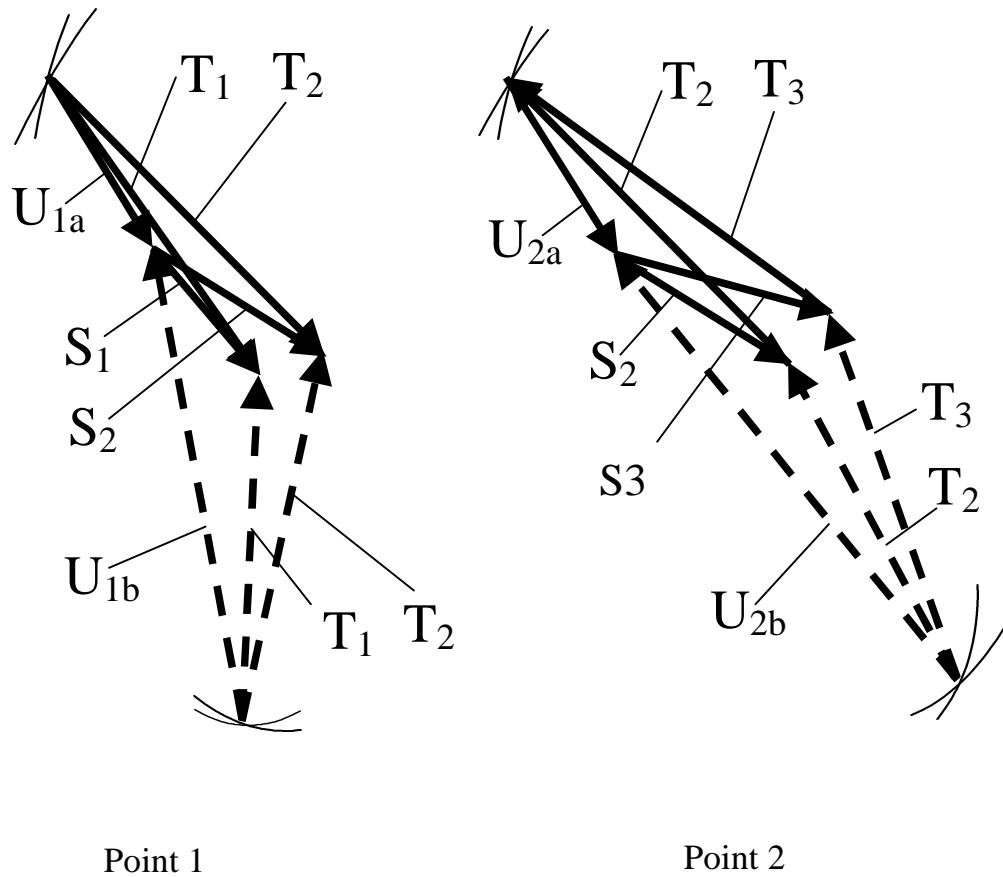
Point 1   Point 2

Fig. 2.5 The complex scattering factors along two pairs of points represented by vectors in the complex plane.

The solution of Eq. 2.4 will be approximately correct in spite of the approximation made in Eq. 2.5 if the rate of change of the reference scattering factor along the Bragg rod is larger than that of the unknown one. This is accomplished by a combination of two means: First, we choose the reference electron density to be similar to the electron density of the real system so that their scattering factors are of the same order of magnitude.

Second, we choose the position of the real space coordinate system so that the CSF of the reference structure will vary more rapidly along the Bragg rods than that of the unknown structure, hence validating the use of the approximation stated in Eq 2.5. Displacing the position of the real space origin say by a vector $\vec{R}_0$ multiplies the Fourier transform of the electron density function by a factor, $e^{i\vec{k}\vec{R}_0}$. This means that, changing the position of the origin in real space affects the Fourier transform phase rate of change in reciprocal space. We therefore choose the origin of the real space coordinate system to be close to the part with the unknown electron density and far from that of the known electron density. Consequently, the phase rate of change of the unknown scattering factor along the Bragg rod is slow in comparison to that of the known part.

2.5.2 Obtaining the electron density

To obtain the electron density we Fourier transform the complex scattering factors function into real space.

2.5.3 Iteration and comparison with experimental results:

The effectiveness of this procedure can be tested in the following way. To qualify as a real electron density, the function obtained from the Fourier transformation of the complex scattering factor function must satisfy certain constraints: It must be real and positive definite and it should go to zero outside the film. In general the function we obtain from the Fourier transformation of the CSF will not strictly satisfy these constraints. So to test how good the result we obtained is we first impose the constraints by zeroing out all the negative parts and the parts that are clearly outside the film. We then use the resulting electron density function to

calculate the diffraction intensities along the Bragg rods. The quality of the agreement between the calculated and experimental diffraction intensities along all Bragg rods is a measure of how close the electron density we obtained is to the real one. If the agreement is not satisfactory one can use the newly obtained electron density as the reference electron density and reiterate the entire procedure to obtain a better result.
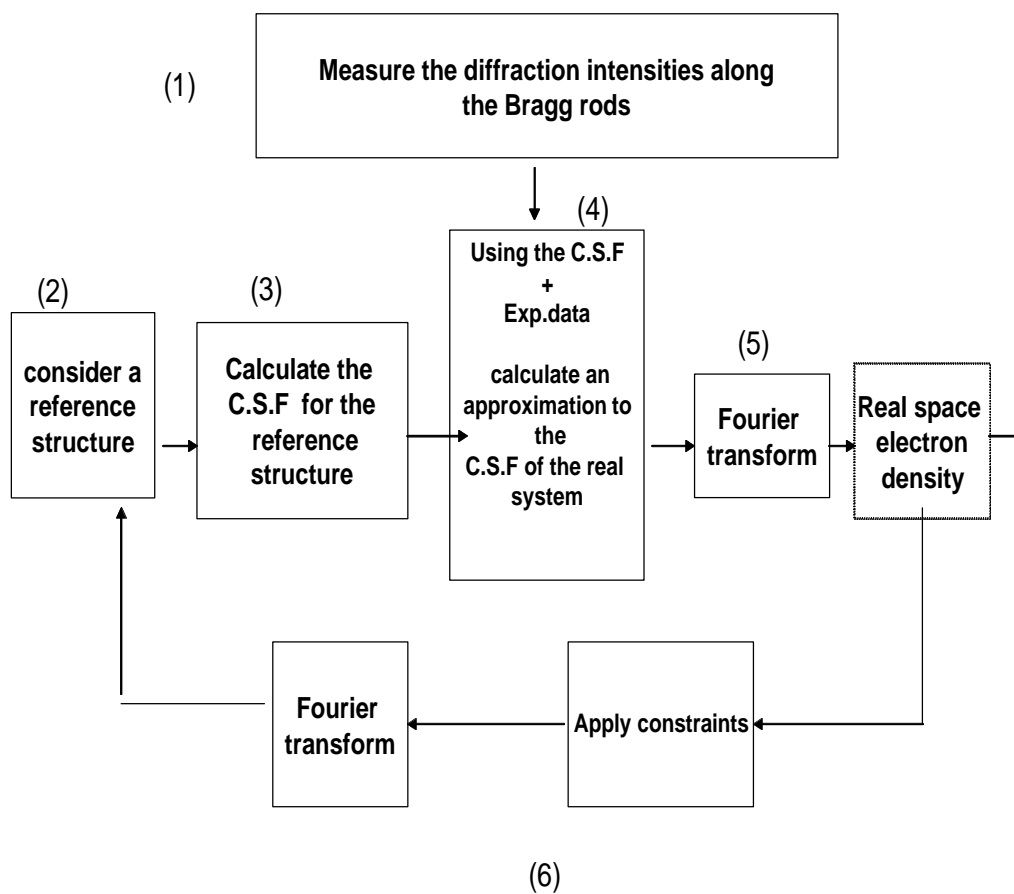
(1) **Measure the diffraction intensities along the Bragg rods**

(4)
**Using the C.S.F
+
Exp.data**

calculate an approximation to the C.S.F of the real system

(2)
consider a reference structure

(3)
Calculate the C.S.F for the reference structure

(5)
Fourier transform

Real space electron density

Fourier transform

Apply constraints

(6)

Fig 2.6 A digram summarizing the COBRA procedure.

CHAPTER III

The Gd$_2$O$_3$-GaAs interface structure

3.1 Sample Preparation:

The sample was prepared at Lucent technologies Bell Labs using pre-cleaned epi ready (100) GaAs wafers specified to have a low crystalline miscut angle $< 0.1^0$. The GaAs and oxide deposition were done in two separate molecular beam epitaxy (MBE) growth chambers linked together by a transfer module with a background pressure of 6×10^{-11} Torr. The transfer process has been evaluated and there is no evidence for oxygen contamination. Inside the MBE chamber, the GaAs wafer was first heated to 580-600^{0}C in an As flux to remove the native oxide from its surface. GaAs deposition was then done using pyrolytic boron nitride effusion cells for the elemental Ga and As. The deposition rate was approximately 0.75-1.0 µm/hr and 0.3- 0.5µm of GaAs was deposited with the surface being gallium stabilized (i.e. contains at least 70% more Ga than As atoms). Under this condition it has been demonstrated that the surface exhibits a (4 x 6) reconstruction[45,46]. The surface reconstruction is assumed to promote single domain growth because it removes the two fold degeneracy of aligning the (110) Gd$_2$O$_3$ plane of rectangular symmetry onto the square symmetric GaAs (100) surface. It was shown that an arsenic stabilized surface, with its associated (2 x 4) reconstruction, also works but the surplus arsenic is more volatile. Once the growth of the GaAs was completed, the wafer was transferred to the oxide MBE chamber. As described elsewhere 45, the gadolinium oxide was deposited from a powder-packed source using electron beam evaporation. The substrate temperature was held at 550^{0}C and the deposition rate was ~ 0.1 µm/hr. During deposition, in-situ reflection high-energy electron diffraction (RHEED) was used to monitor the growth

process.   Analysis of the two-fold symmetric RHEED patterns indicated that the Gd_2O_3 film is (110)-oriented and grown in a single domain.

Once processed, the thickness of the oxide layer was measured by ellipsometry and x-ray reflectivity .For the sample discussed here it was found to be 32Å.

3.2 Sample Properties:

Previous studies by Kortan et al.[42] using X-ray diffraction and secondary electron imaging have confirmed that under the growth conditions described in section 3.1, Gd_2O_3 grows as a cubic single crystal single domain film. The Gd_2O_3 <110> axis is perpendicular to the (100)   GaAs substrate fig3.1. The <001> Gd_2O_3 direction coincides with the <011> GaAs direction with three Gd_2O_3 cell edges matching approximately four GaAs face diagonals with mismatch of -1.9%, while the orthogonal <1-10> Gd_2O_3 direction coincides with the <0-11> GaAs direction with one Gd_2O_3 face diagonal matching approximately 2 GaAs face diagonals with a mismatch of +4.1% fig 3.2.

One should know that Bulk GaAs has a Zinc Blende structure , space group F bar4 3m, with a lattice parameter a_0 at 300K of 0.5653 ,While the Gd_2O_3 has a cubic structure with lattice parameter at 300 K of 1.0813 nm.
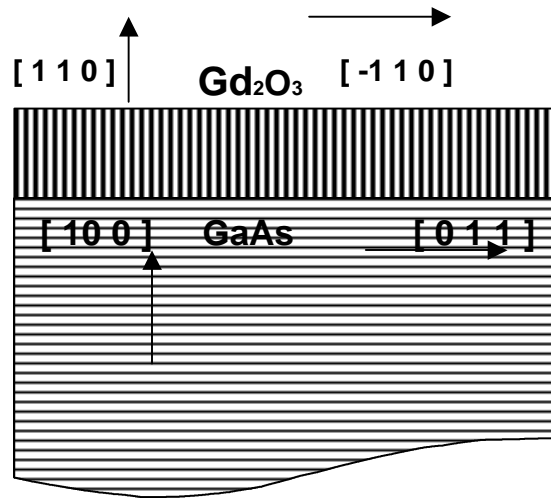
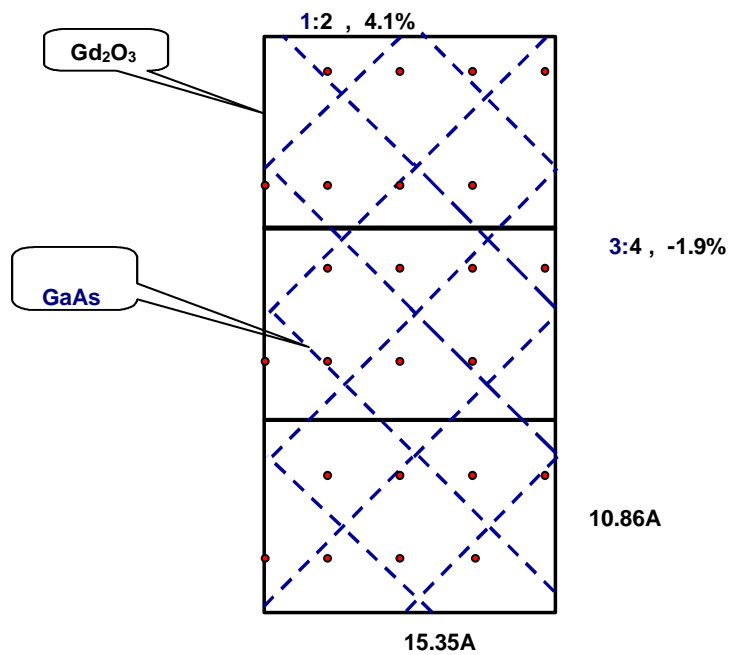fig3.1. Crystallographic orientations of the Gd_2O_3 film and the GaAs crystal.

fig3.2 Gd positions in the first monolayer, Top view. The Gd_2O_3 cell is represented by the solid rectangles. The short side is the Gd_2O_3 cell edge. The long side is the unit cell face diagonal. The dashed lines represents the GaAs 2D unit cells. The mismatch

in the vertical direction is -1.9% while the mismatch in the horizontal direction is 4.1%.

3.3 The Experimental Results:

The 10 keV incident beam allowed us to measure all the Bragg rods within the range $|k| \leq 3; \quad |l| \leq 3$ and $0.1 < h \leq 3.5$. We measured the diffraction intensities along *12 symmetry inequivalent Bragg rods,* h 1 -1, h 0 0,h 1 1, h 0 -2, h 2 0, h 2 -2, h -2 -2, h 3 1, h 3 -1, h-1-3,h -3 -3 , h 3-3, in addition to h-1 1. It turned out that the diffraction intensities along rods with k+l odd were too small to be measured ,only [h 1-1] fig3.3 and [h 0 0] fig3.4 showed pronounced Gd_2O_3 contributions (see the appendices for other experimentally measured Bragg rods). All the others although affected by the film did not show features that could be directly identified with the Gd_2O_3 film. The dark noise was usually about 4 orders of magnitude smaller than the largest intensity along the Bragg rod contributed by the Gd_2O_3 film see fig3.3.

The normalized diffraction intensity along the [h 1 -1] Bragg rod are shown in fig3.3 , The large peaks correspond to [1 1 -1] and [3 1 -1] GaAs substrate Bragg peaks. The broad peak at approximately [1.48 1 -1] and the overtones are due to the Gd_2O_3 film. To verify that this peak is not just the tail of a larger peak at a position off the Bragg rod we performed a scan perpendicular to the rod. In GaAs reciprocal lattice coordinates bulk Gd_2O_3 would have a Bragg peak at approximately [1.48 1.04 -1.04]. The diffraction intensity along the [1.48 ζ $-\zeta$] line that goes through this point is shown in fig3.5. As seen the system has indeed a broad peak at that position but it has a much larger peak on the Bragg rod namely at [1.48 1 -1]. The diffraction intensities along the [h -1 1] Bragg rod were found to be equal to within the experimental accuracy to those on [h 1 -1] while those on [h 1 1], shown in Fig3.6, were completely different. These results confirm the conclusion of Kortan et al[42]. that

the system is single crystal, single domain with 180° rotation but no 90° rotation symmetry.
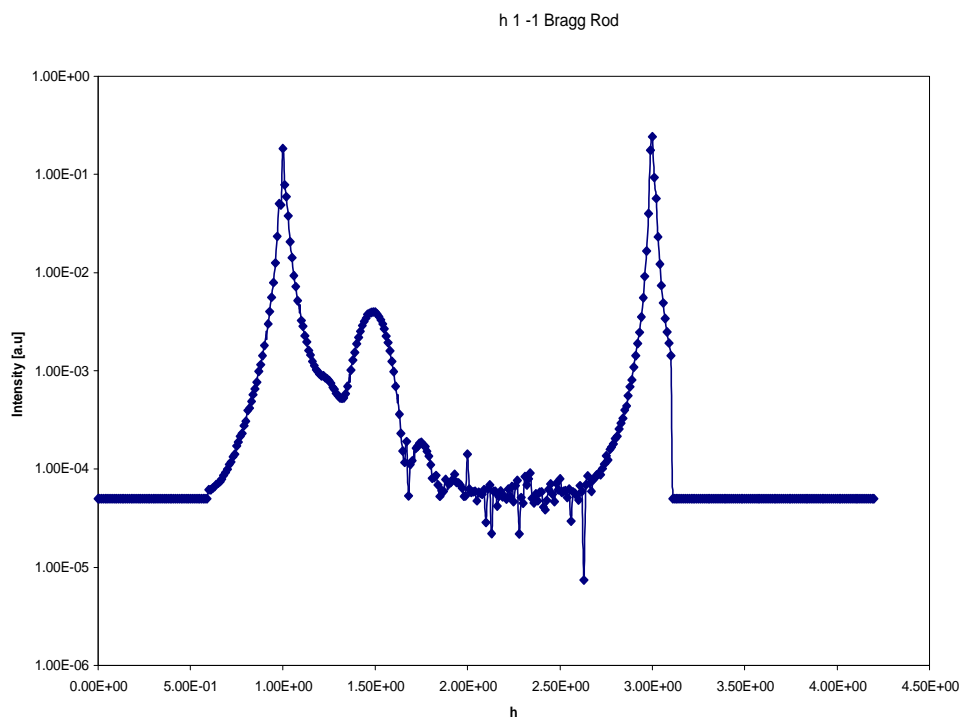
h 1 -1 Bragg Rod

Fig3.3. The normalized diffraction intensities along the [h 1 -1] Bragg rod (logarithmic scale)as a function of reciprocal space lattice units.
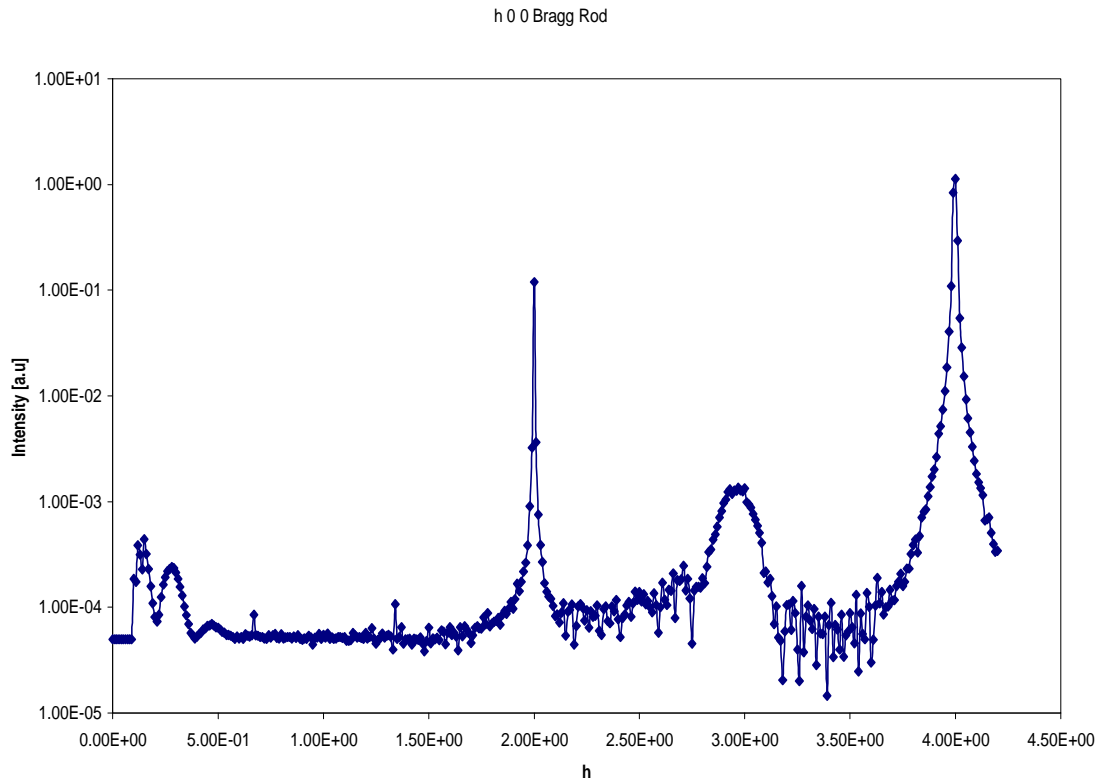
h 0 0 Bragg Rod

Fig3.4. The normalized diffraction intensities along the [h 0 0] Bragg rod (logarithmic
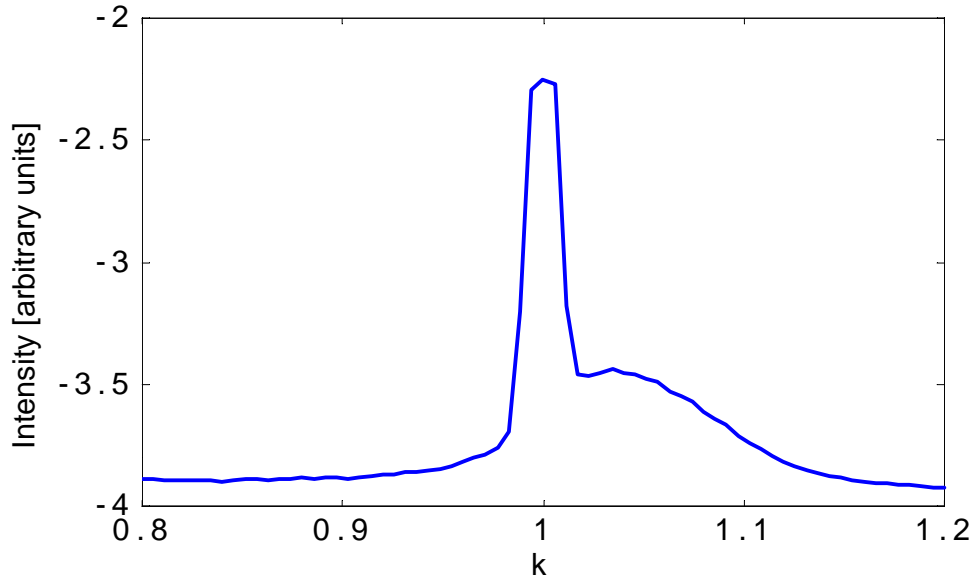
scale) as a function of reciprocal space lattice units.

Fig 3.5. The diffraction intensity along the [1.48 ζ −ζ] line perpendicular to the [h 1 - 1].
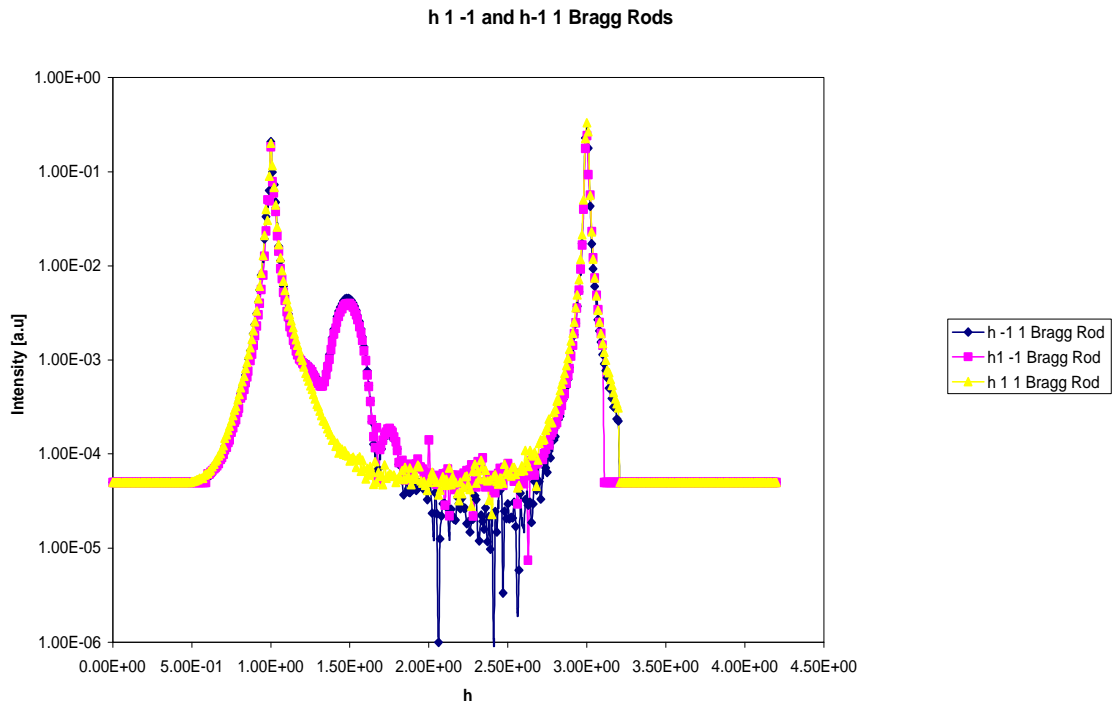
Fig 3.6. The normalized diffraction intensities along the [h 1 -1],[h-1,1] and [h 1 1] Bragg rods (logarithmic scale) as a function of reciprocal space lattice units.

CHAPTER IV

Data Analysis

4.1 The Reference Structure (The Model):

For the determination of the complex scattering factors of the system we need to choose a known structure that is similar to the structure of the system under investigation. We chose to construct a crude model of the system. The model is based on the results obtained by Kortan et al[42]. and consists of the semi-infinite GaAs crystal and a cubic Gd_2O_3 film on top of it. The film is slightly distorted so that 3 Gd_2O_3 unit cell edges match 4 GaAs unit cell face diagonals and 1 Gd_2O_3 face diagonal matches 2 GaAs face diagonals. The Gd and O atoms form, approximately ,layers parallel to the interface. Each layer contains both Gd and O atoms. The largest vertical distance between the Gd atoms within one layer is 0.457A. Four such layers contain all the atoms of one unit cell. We shall concentrate our discussion, mainly, on the Gd atoms. The oxygen atoms cannot be clearly seen due to the fact that they have only 8 electrons in comparison to the 64 of Gd.

Notice that since the period of the Gd_2O_3 is not equal to that of the underlying GaAs, we do not expect to obtain the structure in Fig 3.2. Instead we expect to obtain the folded structure where all the atoms of the combined cell are folded into one GaAs unit cell. The folded structures of four consecutive mono-layers can be seen in Fig 4.2.
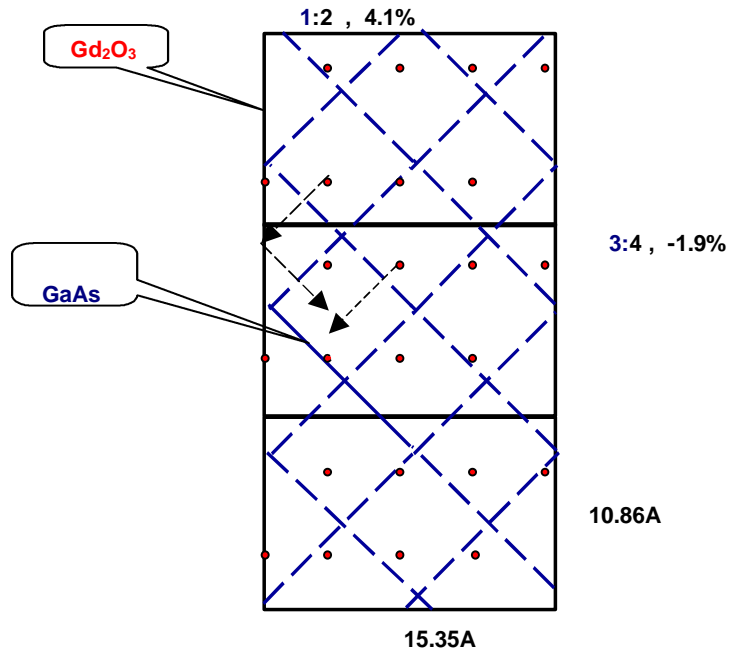
fig 4.1 Gd positions in the first monolayer (top view) ,and the folding procedure using the GaAs 2D reciprocal unit cell vectors which are marked by the arrows.
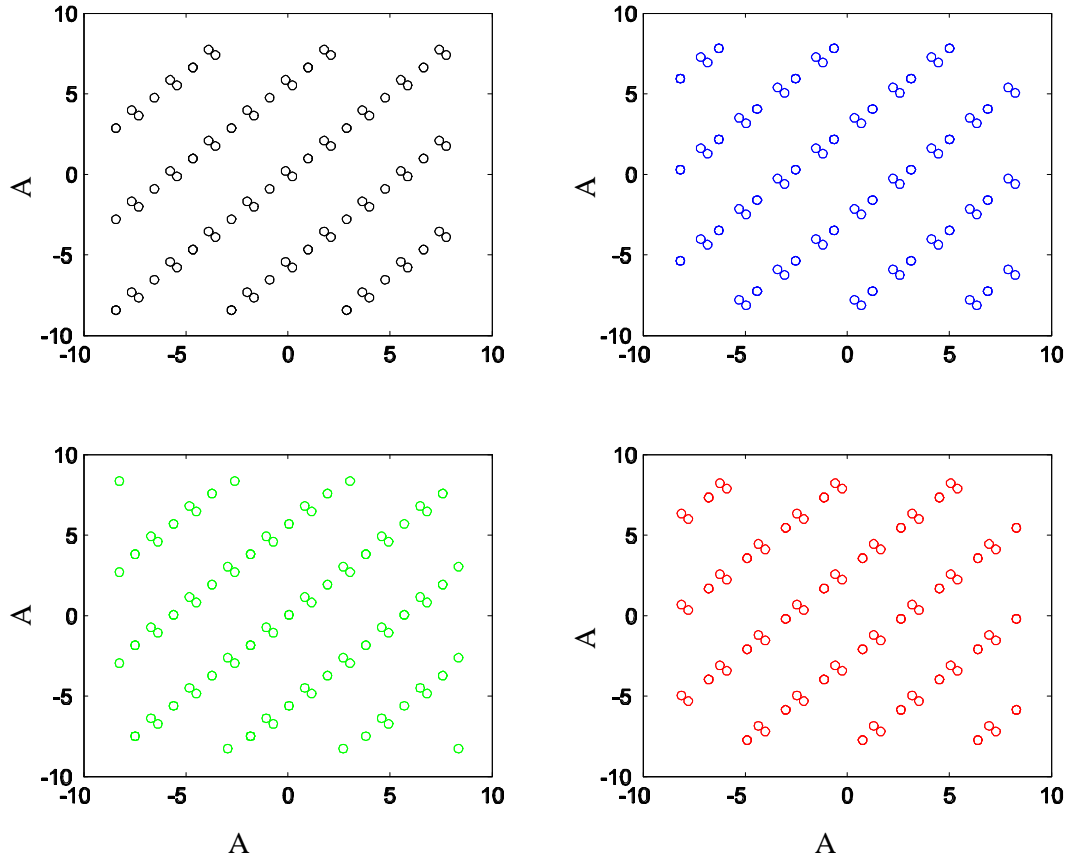
fig 4.2 The folded structure of four consecutive Gd monolayers 12-15. (A=Angstrom)

To make the model somewhat more realistic we introduced a number of variable parameters. These include an overall intensity factor I, a factor u_r multiplying the Gd_2O_3 repeat distance perpendicular to the surface and the number of mono-layers n. Due to the mismatch between the film and the substrate the atoms after being folded, are not expected to be in their ideal positions. We assumed that their distribution about their ideal position is Gaussian with a width S. We used three such parameters: S_{ga} for the GaAs substrate, and S_{yz} and S_x for the distribution in

the Gd_2O_3 film plane and perpendicular to it. Finally, three additional parameters were used to move the film relative to the substrate. So the variable parameters are the following:

1- Over all intensity factor I.

2- Bulk GaAs DW factor S_{ga} .

3- Perpendicular displacement of Gd_2O_3 dx.

4- In- plan displacement of Gd_2O_3 in the y direction dy.

5- In- plan displacement of Gd_2O_3 in the z direction dz.

6- Gd_2O_3 DW factor in the perpendicular direction S_x

7- In-plane Gd_2O_3 DW factor S_{yz} .

8-Vertical Gd_2O_3 layer spacing multiplying factor u_r .

9- The number of Gd_2O_3 monolayers n.

The model parameters were first refined by best fitting the Bragg rod diffraction intensities using the traditional least square method. The results were as follows: u_r =0.946, n=16, S_{ga} =0.35Å, S_{yz} =0.93Å and S_x =0.98Å. The film displacement parameters were found to be such that the ridges of the folded Gd atom positions in the first Gd_2O_3 monolayer overlaps the positions of the Ga or As atoms at the top substrate layer. The fits were found to be insensitive to a motion of the film parallel to the ridges. This is a result of the fact that due to the large S_{yz} the electron density along the ridges varies very little.

The quality of the model was checked by comparing the diffraction intensities calculated from this model with the experimental results. As seen in fig 4.3 the fits are

rather poor. This is true also of all other rods. It is therefore clear that this model is indeed very crude.
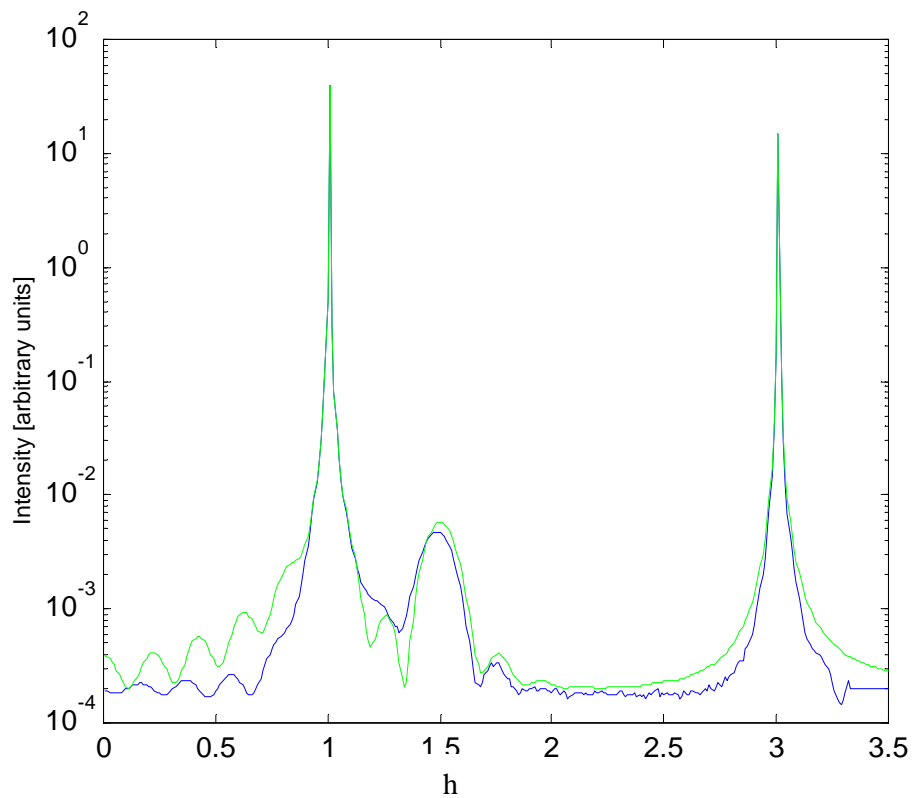

Fig 4.3 The diffraction intensity along the [h1-1] Bragg rod (logarithmic scale) as a function of the reciprocal space lattice units. Blue-experiment, Green-fit curve.

4.2 Determination of the Complex Scattering Factors (CSF's):

Following the procedure discussed in Chapter 2 we used the complex scattering factors obtained from the model as the known scattering factors S and calculated the amplitude and phase of the unknown scattering factors U and of the total scattering factors T of the true electron density. The measurements and the calculations were done only for $h > 0$. The complex scattering factors for $h < 0$ were calculated from the general relation that the scattering factor at $\vec{k}$ is equal to the complex conjugate of the scattering factor at $-\vec{k}$. The scattering factors of the unknown part near the region $(h_b - 0.05) < h < h_b + 0.05$, where h_b is the z component of a Bragg point.

Notice that since the system has 180° rotation symmetry the scattering factor at $T(k_x, k_y, k_z) = T(k_x, -k_y, -k_z)$. Thus, the Fourier transform along each Bragg rod is real and of course the electron density calculated by the Fourier transformation of the complex scattering factor function is real. However, it is not necessarily positive definite. So, to check the quality of the electron density obtained we zeroed out all the negative parts and the parts outside the sample and then used the resulting positive electron density to calculate the diffraction intensity along the Bragg rods. The results are shown in Figs. 4.4,4.5 and 4.6. Notice that in contrast to the model the results obtained from the COBRA analysis are in very good agreement with experiment over two orders of magnitude in intensity.
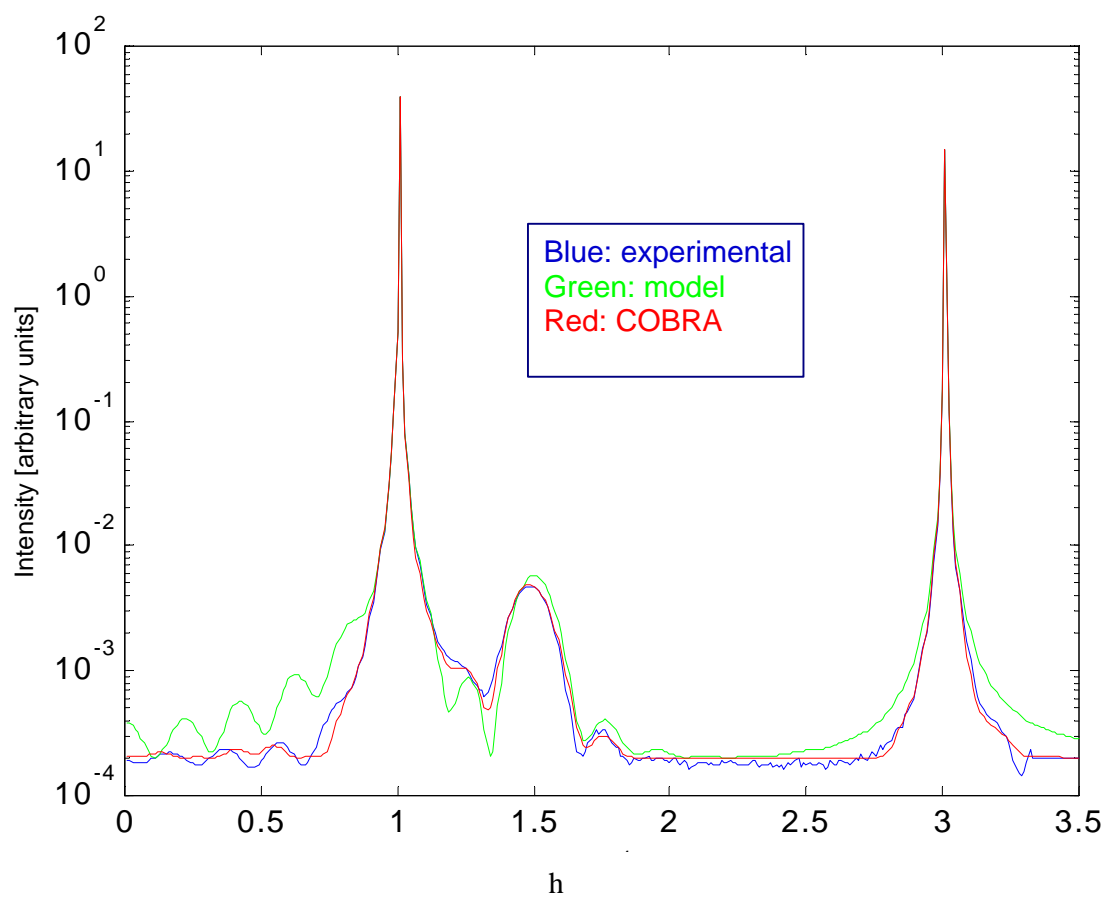
Fig 4.4 The diffraction intensities along the [h1-1] Bragg rod (logarithmic scale) as a function of reciprocal space lattice units.
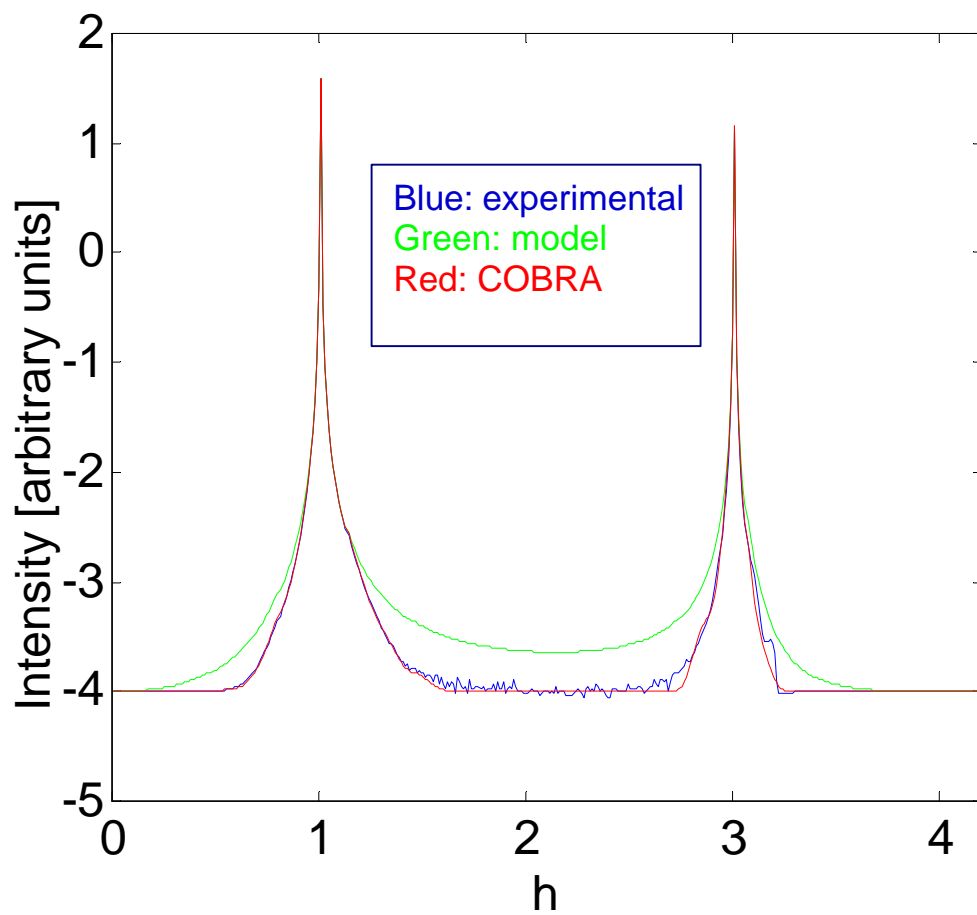
fig.4.5 The diffraction intensities in log scale along the [h 1 1] Bragg rod as a function of reciprocal space lattice units.
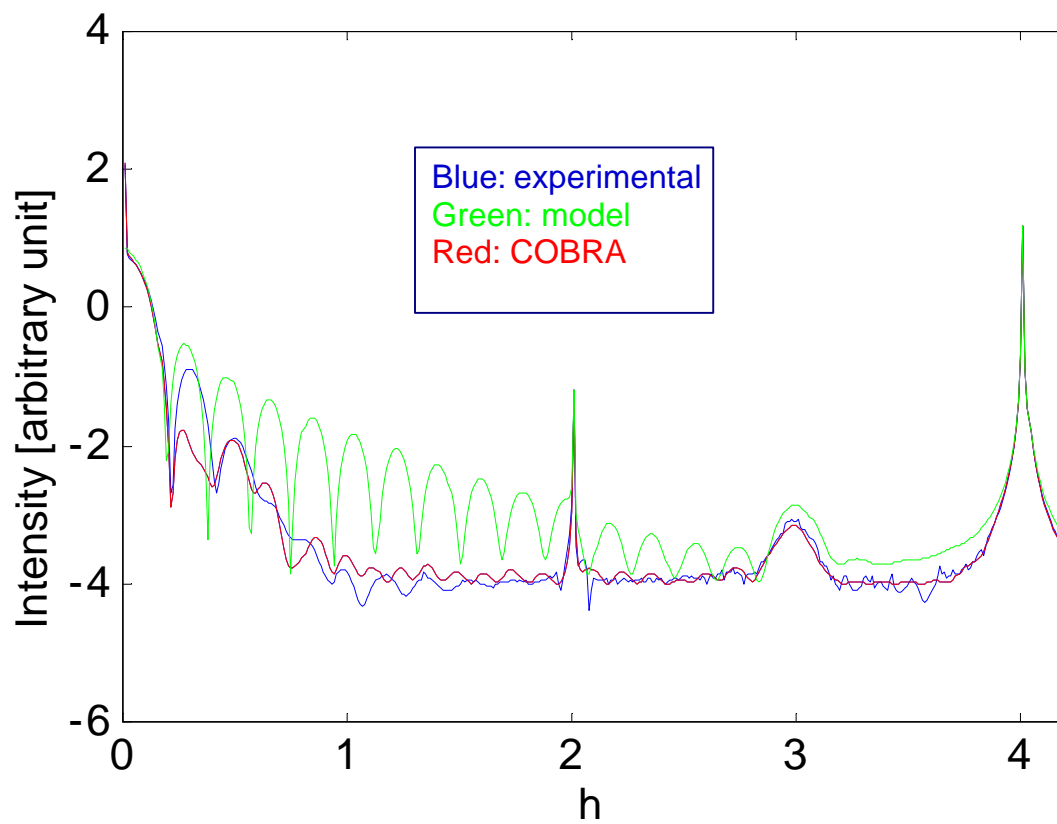
Fig 4.6 The diffraction intensities in log scale along the [h 0 0] Bragg rod as a function of reciprocal space lattice units.

4.3 The Iteration Procedure:

Furthermore, to check the iteration procedure we carried out one iteration. We used the newly obtained electron density as the new known part of the electron density and then calculated the new complex total scattering factor function. The new electron density was obtained by Fourier transforming the complex scattering factor function into real space. As before, we zeroed out the negative parts and calculated the scattering intensity along the Bragg rods. One Bragg rod is shown in Fig 4.7 and as seen the fit quality improves a little. Similar small improvements were observed in all other Bragg rods, but the electron density did not change significantly.
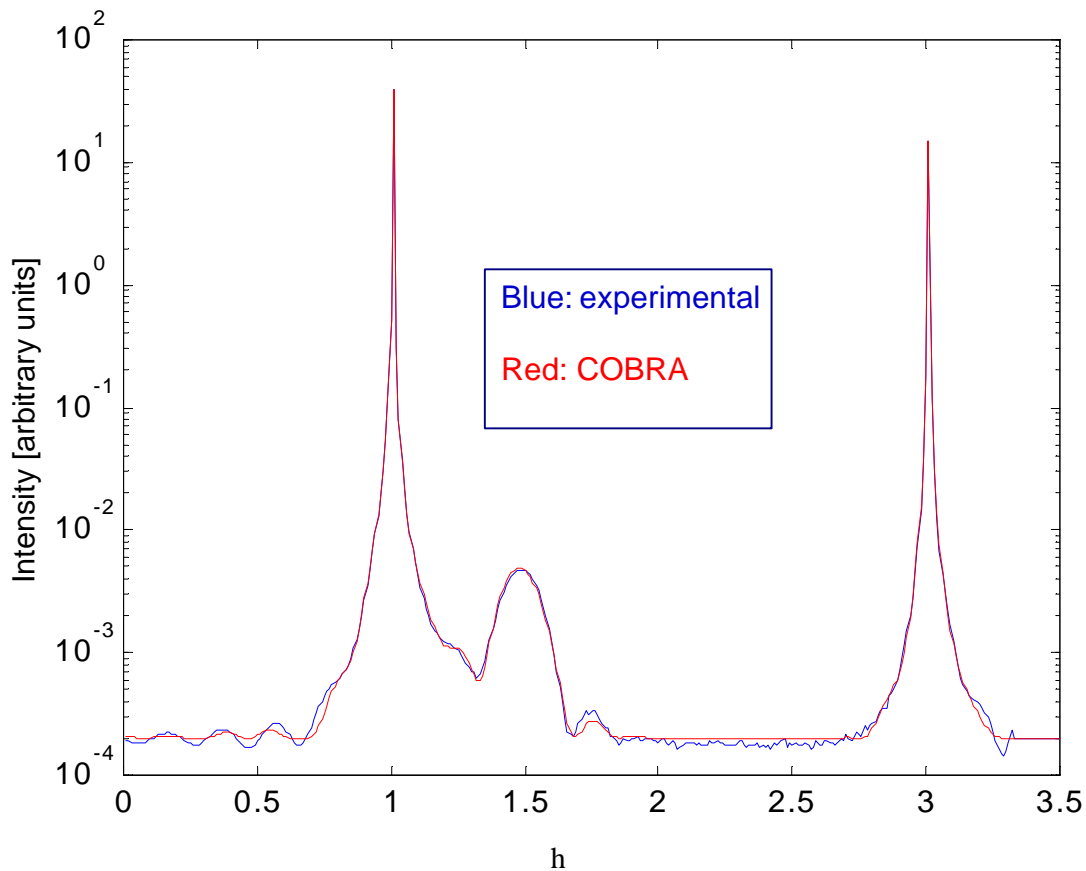
Fig 4.7 The diffraction intensities along the [h1-1] Bragg rod (logarithmic scale) as a function of reciprocal space lattice units after one iteration

CHAPTER V

Results and discussion

Before interpreting the electron density function, obtained by Fourier transformation of the complex scattering factors, in terms of the atomic structure we need to take several considerations into account. First, the range in reciprocal space where we have data is approximately 7 reciprocal space lattice units. This means that the narrowest features possible in the electron density function will have a half width equal to the GaAs unit cell divided by 2 times the reciprocal range, namely 0.35Å. In calculating the Fourier transform we increased the range in reciprocal space by a factor of 3, padding the extra range with zeros. This increased the point density in the electron density function but of course, it did not increase the resolution. Second, regions of the film which are incommensurate with the substrate give rise, when folded, to a uniform electron density. The portion of the film that is incommensurate may vary as a function of the distance from the interface. Other contributions to a background electron density may be due to inaccuracies in the phase, to a slight miss-cut of the surface relative to the crystallographic planes, and possibly other sources.

5.1 The Layered Structure

The in-plane average electron densities obtained from the model and COBRA calculations as a function of distance from the interface are shown in Fig 5.1. The 9 peaks on the left correspond to 9 mono-atomic layers of Ga and As. Ga and As cannot

be distinguished because their atomic numbers differ only by 2. The larger electron density on the right corresponds to sixteen Gd_2O_3 mono-layers. In the model we have assumed an abrupt change from GaAs to Gd_2O_3 and an abrupt end of the film. The COBRA electron density shows that the transition is gradual over approximately five mono-layers. The transition region may be either a result of interface roughness or Gd diffusion into the GaAs. The fact that the surface roughness is also about 5 mono-layers suggests that the transition region is a result of interface roughness. We suggest that the GaAs substrate had ,probably, about 5 mono-layers of roughness to begin with. This led to five mono-layers of interface roughness and finally to five mono-layers of surface roughness.

Notice that on the left, far from the interface within the GaAs substrate, the peak to valley ratio in the COBRA calculated electron density is large and corresponds to a Gaussian distribution $Ae^{-x^2/(2s^2)}$ with $s = 0.35$ Å. As pointed out, this is the minimal value expected since the data extends out to only $|h|,|k|,|l| = 3.5$. Going to the right into the Gd_2O_3 film, the peak to valley ratio decreases leading to an increase of s . The peak to valley ratio in the Gd_2O_3 film is about equal to that of the model. So, $s \approx 0.9\,A$. This value is much larger than the resolution and is probably a result of the strain present in the film.
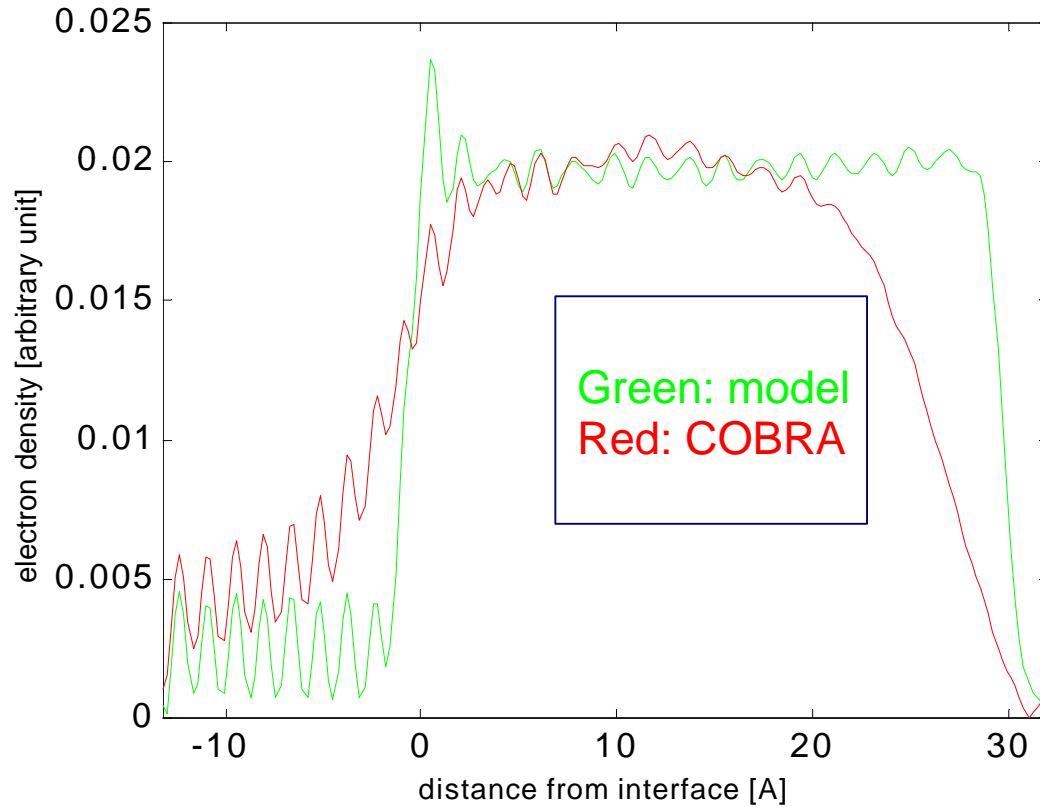
Fig. 5.1 The in-plane average electron density as a function of distance from the interface (A=Angstrom).

5.2 The n- Plane Atomic Structure

Let us now consider the in-plane atomic structure. The in-plane electron density map of mono-layers -9 and -8 are shown in Figs 5.2a and 5.2b. as I mentioned earlier the layers are numbered with respect to the nominal GaAs/Gd$_2$O$_3$ interface with negative numbers on the GaAs side of the interface. In both layers the Ga and As

atomic positions can be clearly seen and the two maps are shifted with respect to each other as expected for GaAs. The Gaussian half width of these peaks is 0.37 Å, namely similar to the vertical width and caused by the limited resolution of the data.
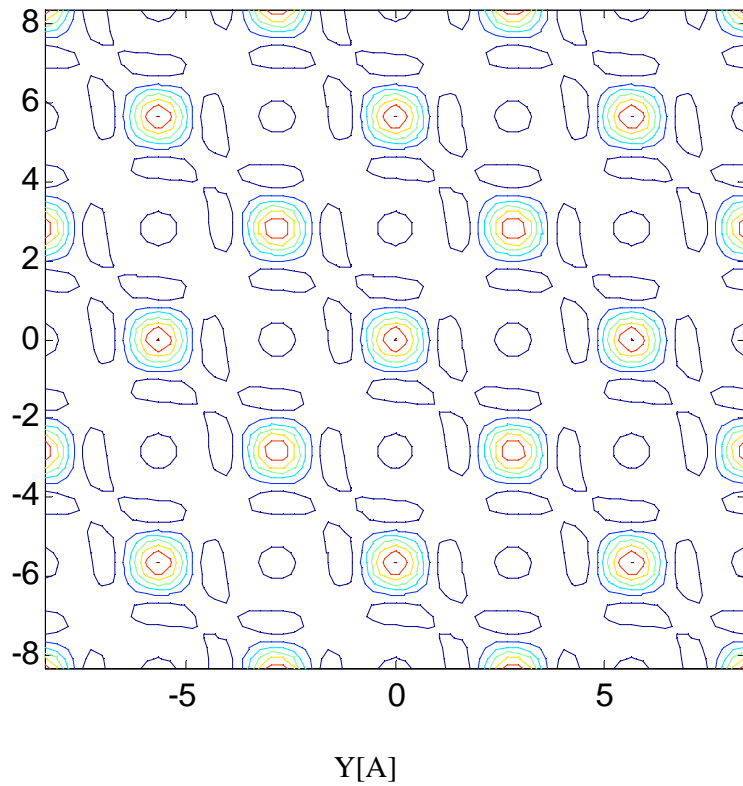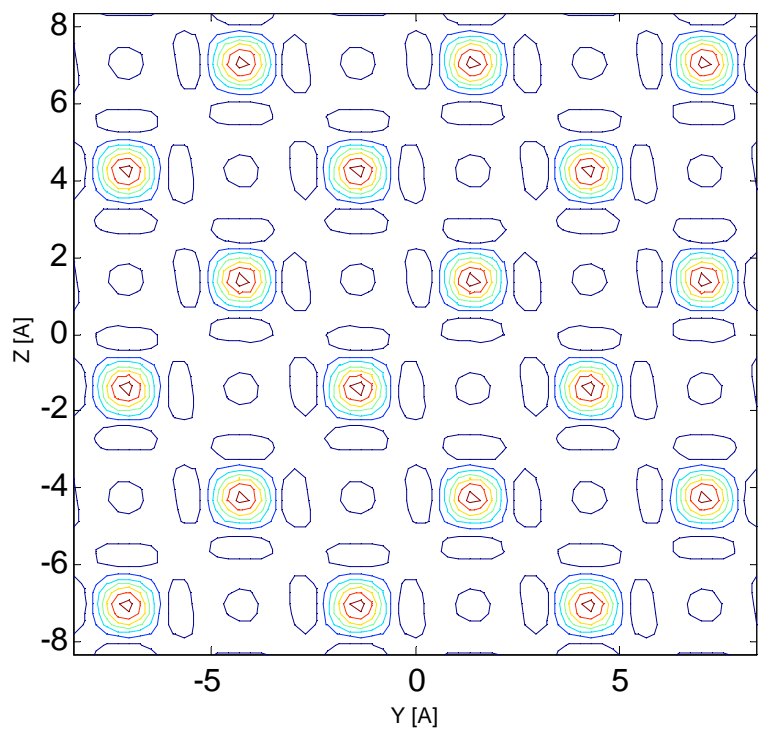
Figs 5.2a ,5.2b the in-plane electron density map of two consecutive GaAs monolayers (A=Angstrom).

An example of the model electron density map on the Gd_2O_3 side (nominally layer +12) is shown in fig.5.3a. This map shows the ridges and valleys expected from the folded Gd positions. However, the electron density along the ridges is almost completely flat. In contrast, the COBRA calculated electron density shown in fig 5.3b shows clear structure along the ridges. To understand this structure we show on the same figure the Gd positions in bulk Gd_2O_3 as black dots. Each dot in a pair of dots represents 2 atoms folded to the same place in the plane but at slightly different positions perpendicular to the plane. Similarly each single dot represents 4 occluded atoms. The large peaks appear at the center between a pair and a single dot. This suggests that the folded atoms are actually closer together than expected from the Gd_2O_3 bulk structure. The smaller peaks are at the positions of one dot or one pair of dots as expected. This behavior is seen in all mono-layers.
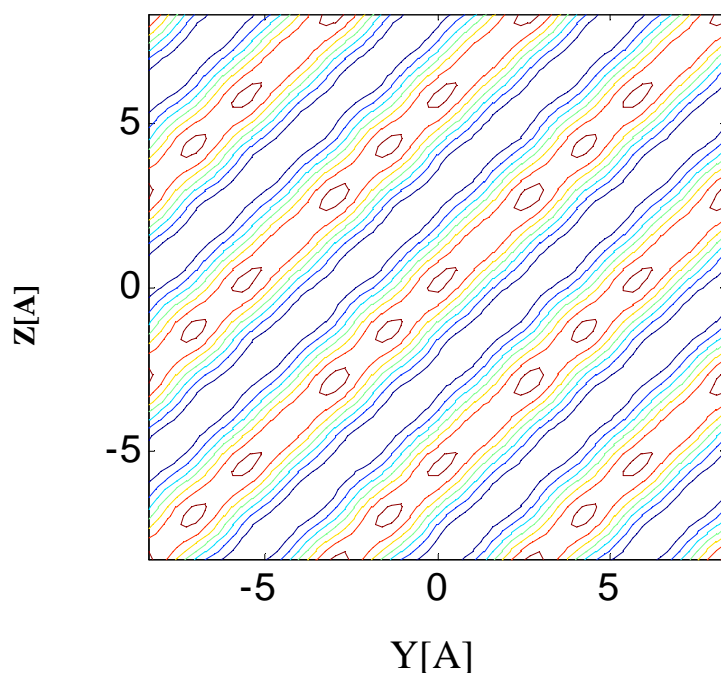

fig. 5.3a The model electron density map of layer +12 at the Gd_2O_3 side (A=Angstrom) .
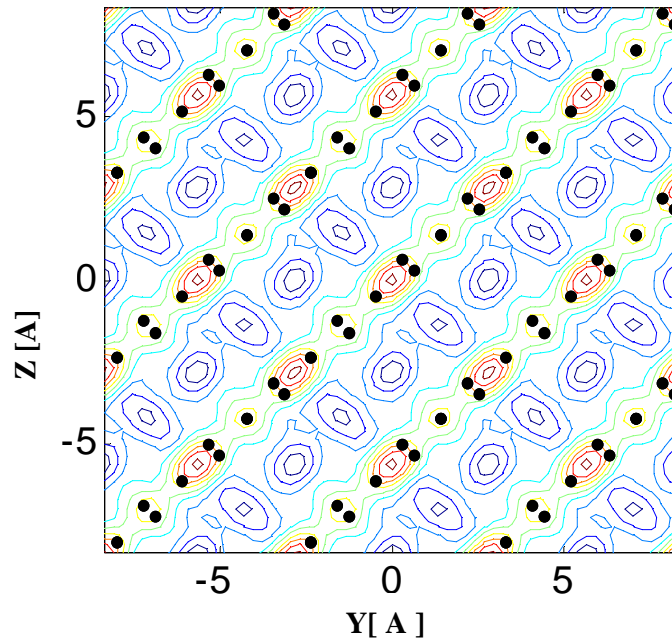
fig 5.3b The COBRA result electron density map of the monolayer +12 at the Gd$_2$O$_3$ side (A=Angstrom).

To determine the displacements of the folded atoms from the peak positions we plotted the electron densities along the ridge centers. An example is shown in fig 5.4. We then fitted the electron density with Gaussian functions. Each group of four atoms (a pair of dots or a single dot) were represented by a Gaussian. The amplitudes and widths of all Gaussians were equal (each representing four atoms) and were allowed to vary together with the displacements of the Gaussians neighboring the large electron density peaks. This gave us 3 variable parameters. Using these parameters we obtained good fits to the electron density distributions. However since we also expected possible background contributions we included this 4th parameter in our fits. These refinements resulted in excellent fits. We did that for all the monolayers on the Gd$_2$O$_3$ side fig 5.5. The displacements and the Gaussian widths are

shown in fig 5.6 as a function of layer number. Since both fits were good, the values

shown in the figure are the averages of the parameters obtained in both fits and the

error bracket is the average difference between the two. The two horizontal bars on

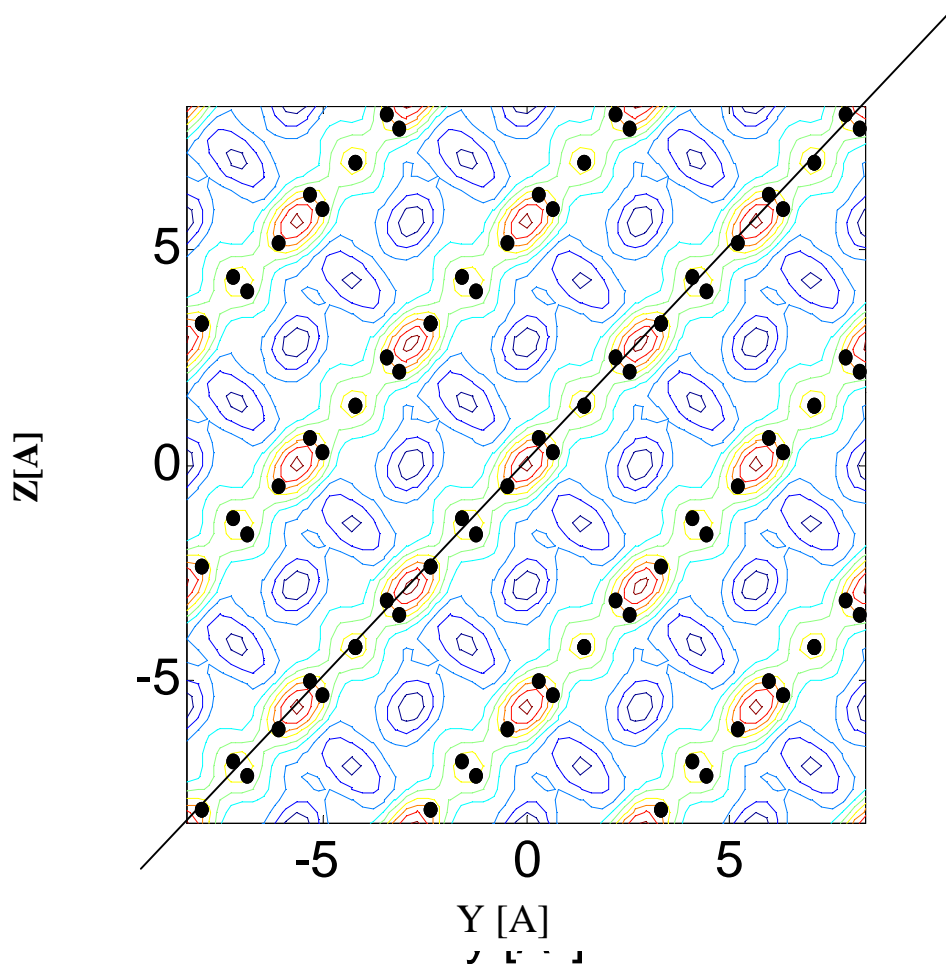the right represent the displacements in alternate layers in the bulk Gd_2O_3 crystal.

Fig 5.4 The electron density map of monolayer + 9 . We perform the fit along along the ridge center (A=Angestrom).
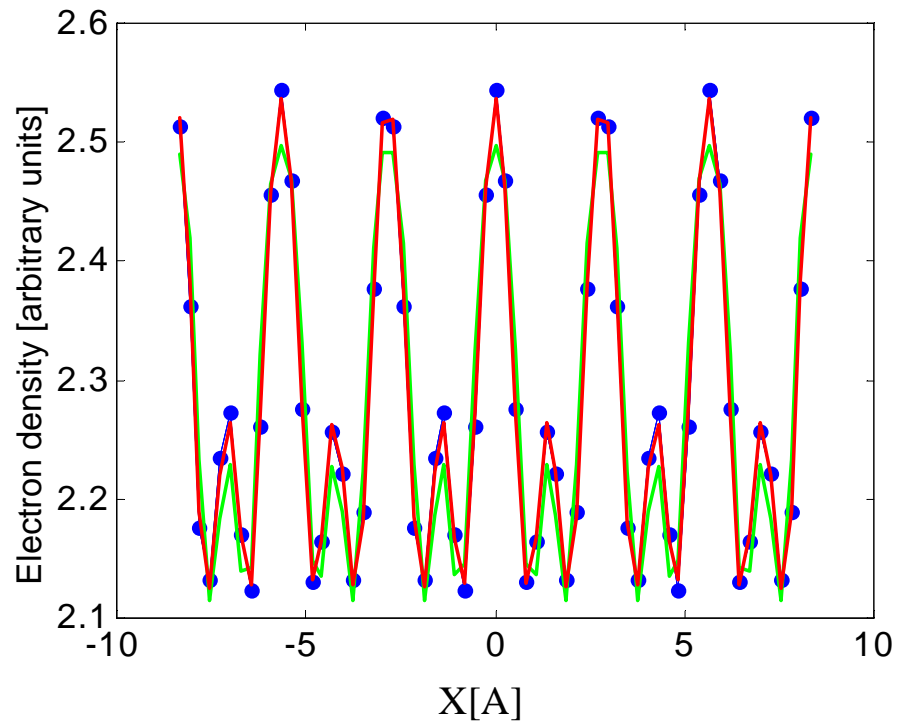
Fig 5.5 Fits to the electron densities along a ridge in layer 9: blue dots-experiment; green curve –fit without background; red curve-fit with background (A=Angstrom).
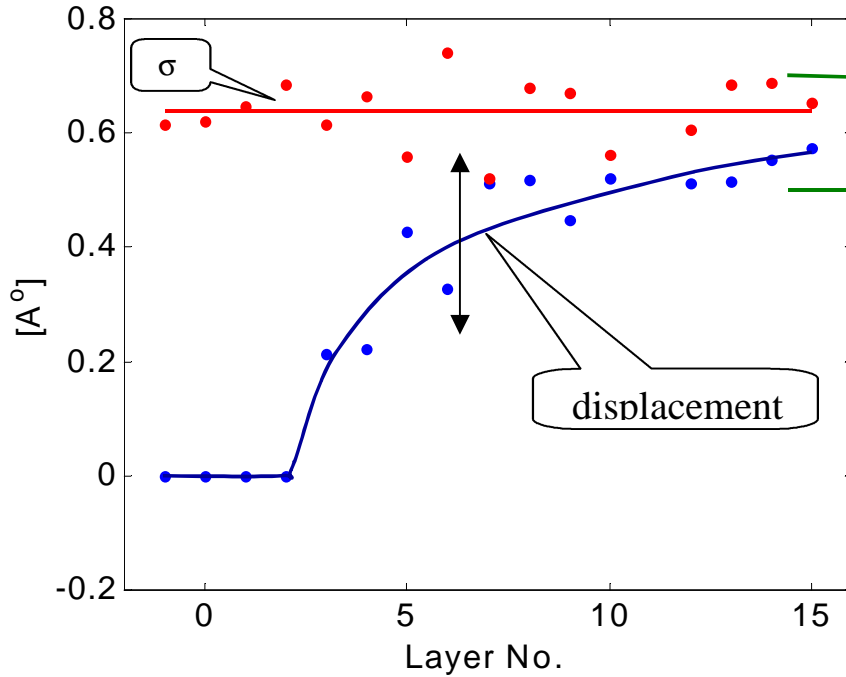
Fig 5.6 The distance between Gaussian peak and the neighboring large electron density peak (blue dots) and Gaussian width (red dots) as a function of layer number.

The results show that in the first 3 layers the in-plane folded positions of each group of 8 atoms coincides with the center position of a large peak in the electron density. As the distance from the interface increases, the displacements increase towards the displacements present in bulk Gd_2O_3. Using a similar approach we found that the Gaussian widths in the in-plane direction perpendicular to the ridges is also

. Notice that these values are smaller than the values found in the initial model.

The repeat distance in the vertical direction is four layers in both GaAs and Gd_2O_3. Let us now consider the four consecutive layers on the Gd_2O_3 side.

Notice that the in-plane atomic positions in each layer are shifted relative to the next layer by a vector shift indicated in the layer. These vectors in the model (bulk Gd_2O_3) fig 5.7a are:

$a(0.08\vec{I}y - 0.42\vec{I}_z)$, $a(-0.25\vec{I}_y + 0.25\vec{I}_z)$ $a(0.42\vec{I}_y - 0.08\vec{I}_z)$ and $a(-0.25\vec{I}_y + 0.25\vec{I}_z)$

$$....(5.1)$$

Here a is the GaAs unit cell, and $\vec{I}_y$ and $\vec{I}_z$ are unit vectors in the y and z directions. The COBRA calculated electron densities in four consecutive layers shown in fig 5.7b are also related to each other in a similar way but the shift vectors are different. They are:

$a(+0.25\vec{I}y - 0.25\vec{I}_z)$, $a(-0.25\vec{I}_y - 0.25\vec{I}_z)$ $a(-0.25\vec{I}_y + 0.25\vec{I}_z)$ and $a(+0.25\vec{I}_y + 0.25\vec{I}_z)$

$$....(5.2)$$

This shows that the stacking order in the film is different from the stacking order in bulk Gd_2O_3. The difference in the stacking order can also be seen in the following way: In fig 5.7a the center point in map a is on a ridge, in b – valley, in c – ridge and in d –valley. In contrast the sequence in Fig 5.7b is a – ridge, b- valley, c – valley, d – ridge. The stacking order shown in fig 5.7b hold throughout the entire film thickness. One should know that the disorder in the atomic positions determined by COBRA method in fig 5.6 can be correlated with the measurements of the X-ray diffuse scattering shown in fig 3.5.

The Gaussian half width k of the broad peak centered at k= 1.04A $^{-1}$ equals 0.05*2*ð/a A^{-1}, and since the Fourier transform of a Gaussian function is another Gaussian we have:

$$A_1 exp(-k^2/2* k^2) \ ---- \ FT ------ \ A_2 exp(-x^2* k^2/2) \ ....(5.3)$$

so the correlation length in real space L = 1/ k= 18   Å.

The mismatch between the GaAs and the Gd_2O_3 is $1/1.04-1=-0.038$ (see fig 3.5).

This means that the disorder in the atomic positions is :

$$\sigma=L*0.038 =0.68\text{Å} \quad \ldots\ldots\ldots\ldots..(5.4)$$

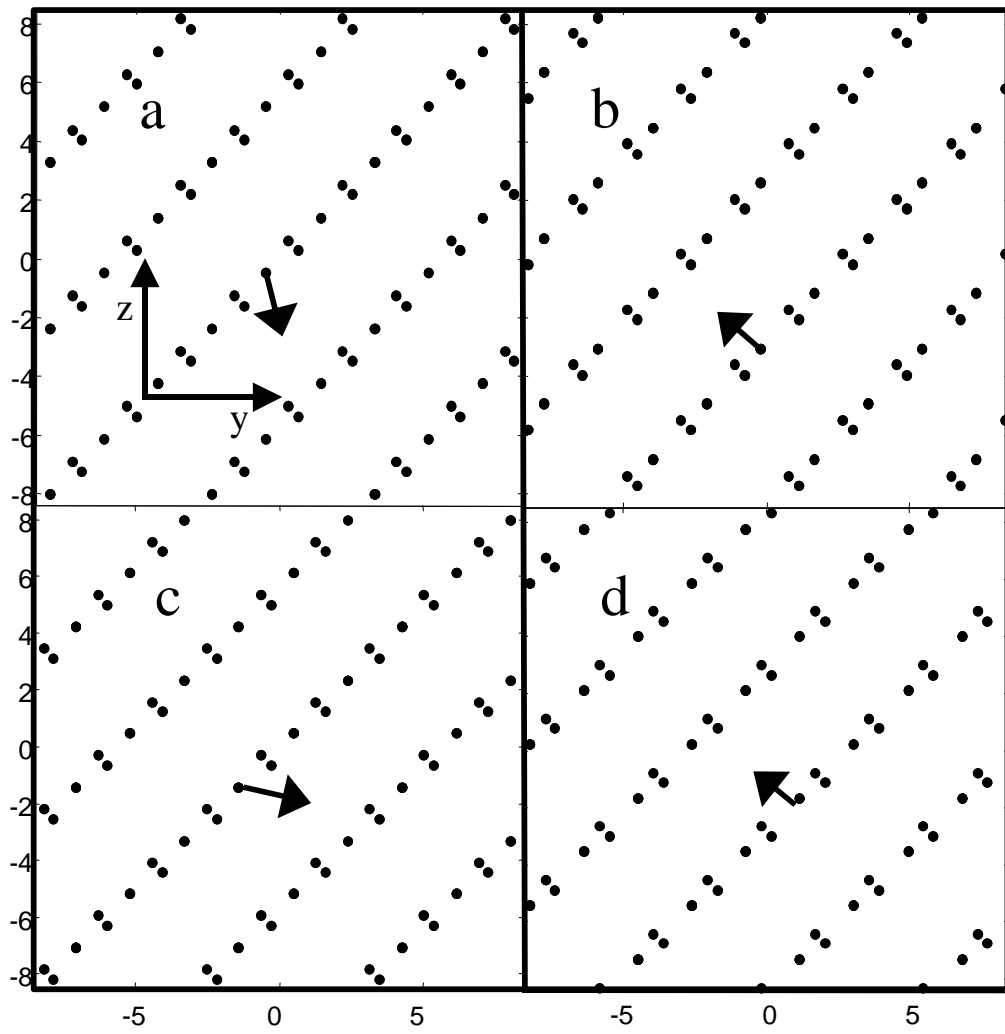This result is consistent with the result obtained by COBRA $\sigma=0.65\text{Å}$.

Fig 5.7a The model in-plane electron density maps of layers 9 through12 (a-d). Each map consist of 3x3 GaAs 2-D unit cells.
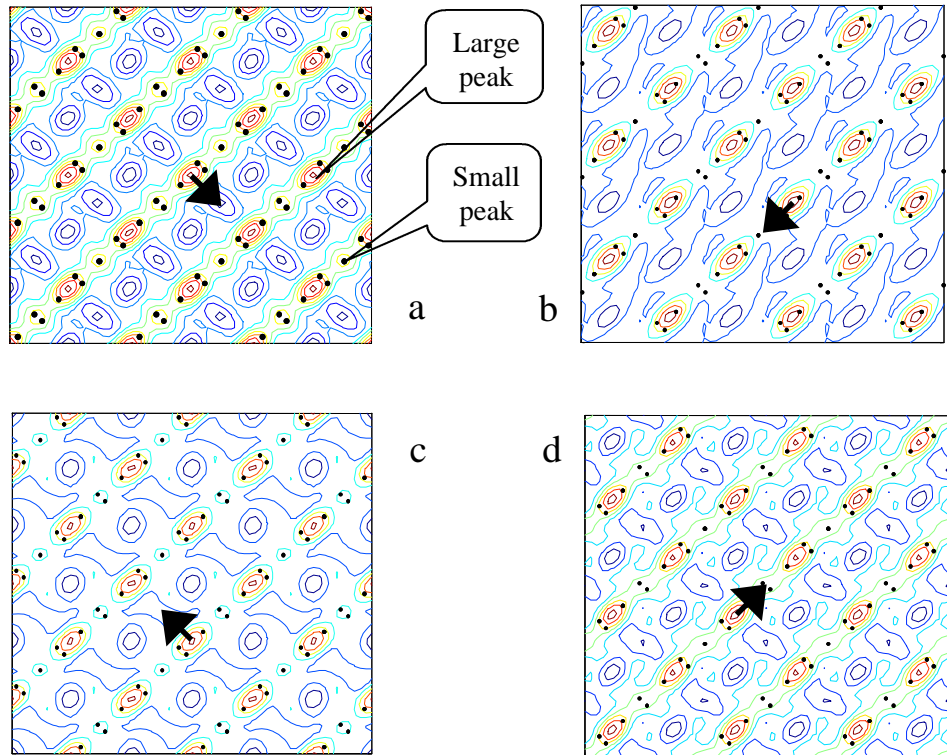
Fig 5.7b The COBRA result in-plane electron density maps of layers 9 through 12 (a-d). Each map consist of 3x3 GaAs 2-D unit cells.

5.3 How accurate and unique is the derived structure?

As I mentioned in section 2.5.3, The quality of the agreement between the calculated and experimental diffraction intensities along all Bragg rods is a measure of how close is the electron density we obtained to the real one. If the agreement is not satisfactory one can use the newly obtained electron density as the reference electron density and reiterate the entire procedure to obtain a better result. As shown in figs 4.4, 4.5, 4.6, the agreement is very good but not perfect.

The sources of errors are:

a) Shot noise. The intensity at the peak of the Gd2O3 contribution was about 10,000 photons. So the noise was 1%. The signal to noise ratio was accordingly smaller in regions of smaller contribution.

b) The systematic experimental errors are:

- due to imperfect intensity calibration estimated at 10%.

- due to imperfect background subtraction. This affects mainly the low intensity regions that almost do not affect the structural results .

c) Inaccuracy of the COBRA analysis. This error is due to the fact that the approximation we make is not ideally satisfied.

The combined effect of all the errors shows up in the mismatch between the measured and calculated diffraction intensities.

 Now the question is how do these errors affects our conclusions?

To answer this question we used the following approach:

1-We took the experimentally measured diffraction intensities of the measured Bragg rods and Fourier transformed them into real space to obtain the ranges that we have a noticeable signal.

2- We considered a vector X with the same dimension of the experimentally

measured Bragg rods, in which the absolute value of each element is one with

randomly changing phase in the range where we have a noticeable signal and zero

else where .

$$X = \quad \exp (i*2*\eth*r_j) \qquad \text{strong signal.}$$

$$0 \qquad\qquad\qquad \text{else where.}$$

(r_j is a random number changing from 0 to 1)

3- We took the fft (Fourier transform) of X, filter the signal with a low frequency

filter to obtain a random signal which changes smoothly between positive and

negative like the mismatches(see fig 4.4).

4- We applied back Fourier transform on the signal obtained from step 3, and

multiplied the result with the difference between the experimentally measured and

calculated diffraction intensities to obtain artificial noise with same order of

magnitude as the mismatches.

5- We took the artificial noise obtained from step 4 and added it to the experimentally

measured intensities, and applied our COBRA procedure as if it is a new experiment

and checked the effect on the final results in comparison with the results of the real

experiment.

We found the following results:

   a) In the in-plane average electron density as a function of distance from the

interface (fig 5.1) we checked how many layers are in the transition region between

the film and the substrate . We found no measurable changes.

   b)We checked the stacking order of the layers inside the film for both cases. We

found that the stacking order did not change.

c) We checked the changes in the displacement of the folded atoms from the peak positions fig 5.6. The results were within the error bar shown in fig 5.6.

CHAPTER VI

Summary and Conclusions

In this work we have shown that the COBRA method provides a detailed 3D electron density map of a rather complex epitaxial system. It is important to emphasize that the electron density we obtained is qualitatively different from the initial model we started with. Furthermore the very good agreement obtained between the calculated and measured diffraction intensities along thirteen symmetry inequivalent Bragg rods is not a result of fitting but a result of the determination of the complex scattering factors. In fact the simple model we started with turned out to be both qualitatively and quantitatively wrong yet the final result is very close to the correct electron density as evidenced from the fact that in addition to satisfying the required constraints it yields diffraction intensities that are in very good agreement with experiment. The final results did not depend on the specific initial model we chose as long as it was reasonable. Namely, the diffraction intensities it yields are of the same order of magnitude as the experimentally measured ones over most of the Bragg rods. We believe this is generally true as it is based on the many simulations that we did, in addition to the measurements reported here.

The electron density we have obtained is that of the folded system. It provides the atomic positions averaged over all 2D unit cells as well as the position probability distribution function, namely, the probability to find an atom at a certain position. The folded structure does not contain information about structural correlations such as pair correlations, the average coherence length of locally incommensurate regions etc. For example, if two adjacent atoms in the unit cell have a certain distribution width, the distance between them in the real system may have a much smaller distribution if

their positions are correlated or up to 2 times larger if their positions are anti-correlated. So, other experimental methods are needed to complement COBRA. Information on correlations can be obtained from diffuse scattering outside the Bragg rods, from XAFS and possibly x-ray holographic methods. However, as mentioned before the information they provide is averaged over atoms of the same species at inequivalent positions throughout the epitaxial film and some of them are open to interpretation.

6.1 Concluding remarks on the Gd_2O_3-GaAs system

The information we now have on the epitaxial Gd_2O_3 film can be summarized as follows:

a) As suggested by Kortan et al[42]., the film structure is cubic and single domain with the [1 1 0] axis of the Gd_2O_3 perpendicular to the surface an its [-1 1 0] and [0 0 1] axes parallel to the GaAs [0 1 1] and [0 -1 1] axes, respectively.

b) At the interface the electron density changes gradually from the GaAs to the Gd_2O_3 over four to five layers. The transition region is probably due to interface roughness. A similar transition region is seen at the surface and is probably due to surface roughness. The fact that the two thicknesses are about equal suggests that the GaAs had this surface roughness to begin with.

c) The strains due to the mismatch between the GaAs and Gd_2O_3 unit cells cause disorder in the folded atomic positions. The distribution width in the GaAs is much smaller than the parallel and perpendicular widths in the Gd_2O_3 film. This is

of course expected because the film is thin. What is surprising is that the width in the planes is significantly smaller than the perpendicular width.

d) The Gd positions in the first few layers are displaced so as to exactly match the positions of the underlying Ga and As. As the distance from the interface increases they relax to the positions expected in bulk Gd_2O_3.

e) The stacking order of the layers in the film is different from that in bulk Gd_2O_3. In fact the main peaks of the folded electron density in each monolayer of the film are exactly at the Ga and As positions in the GaAs and follow the same stacking order.

The last two points indicate that the folded Gd_2O_3 tends to adopt a structure very similar to that of GaAs. This could be at the bottom of the fact that Gd_2O_3 forms a very good passivation layer for GaAs.

### 6.2 Concluding remarks about the method COBRA

1- For a system with 2D period commensurate with the substrate (Gd_2O_3 on GaAs substrate) we can obtain the 3D atomic positions of the folded system.

2- For a system with 2D period equal to that of the substrate ($BaTiO_3$ on $SrTiO_3$) we can obtain the 3D atomic positions.

3-The fact that the phase is calculated at each point using information from neighboring points only, means that the method can handle cells with a very large number of atoms.

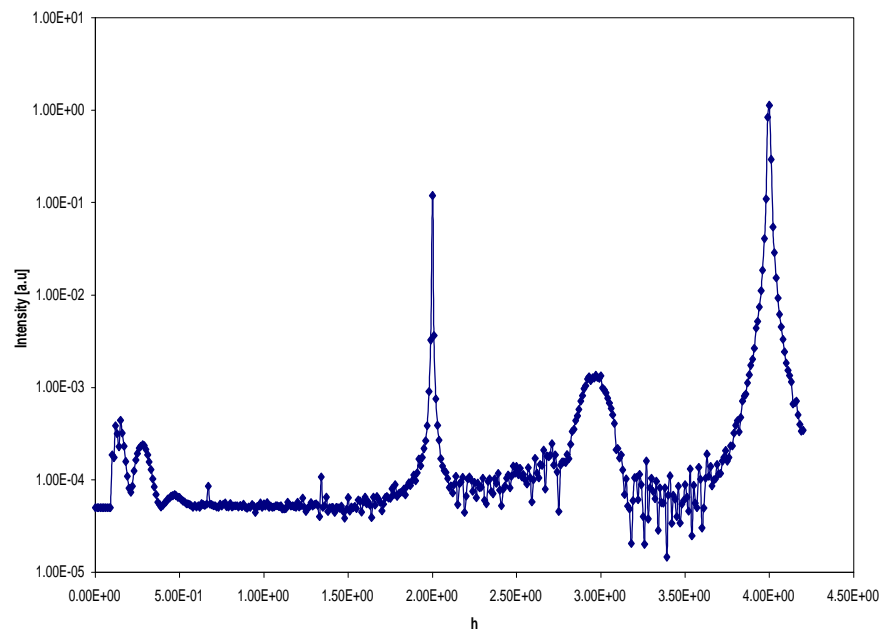4- COBRA is a powerful new method to determine the atomic structure of 2D-systems.

APPENDICES

The diffraction intensities along different Bragg rods (logarithmic scale) as a function of reciprocal space lattice units.
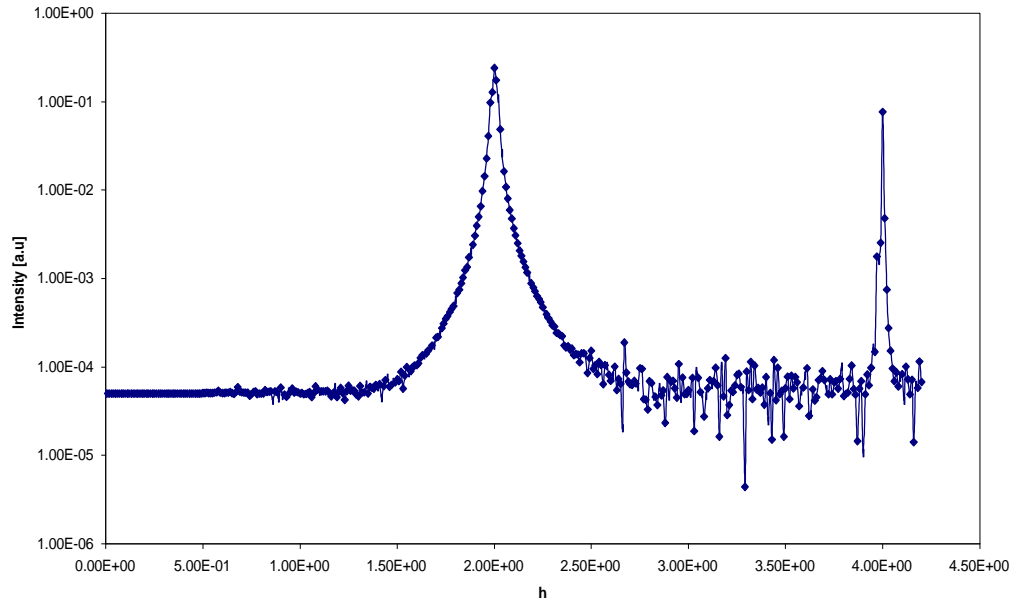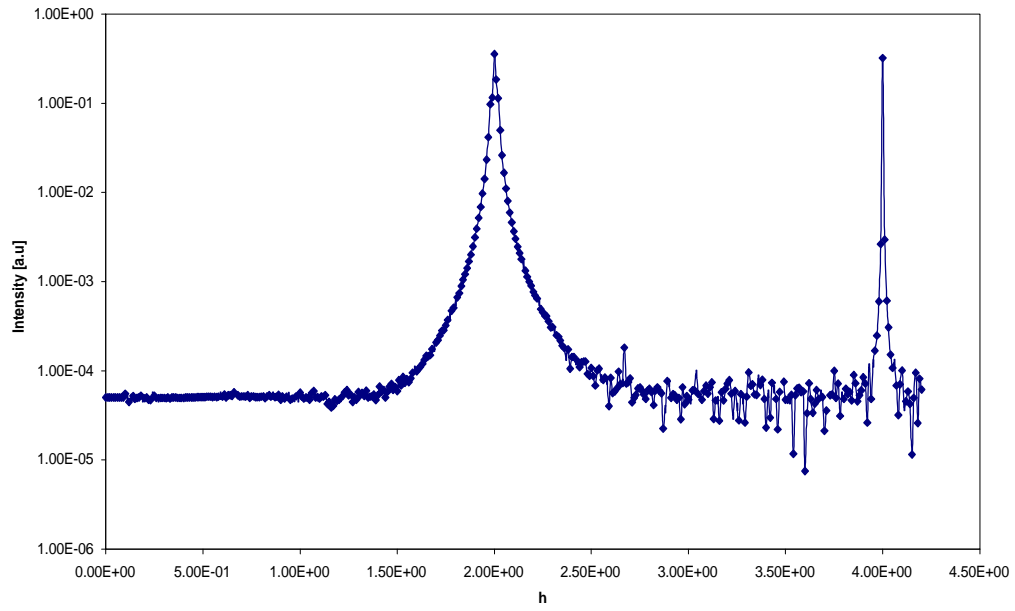

h-11 Bragg Rod
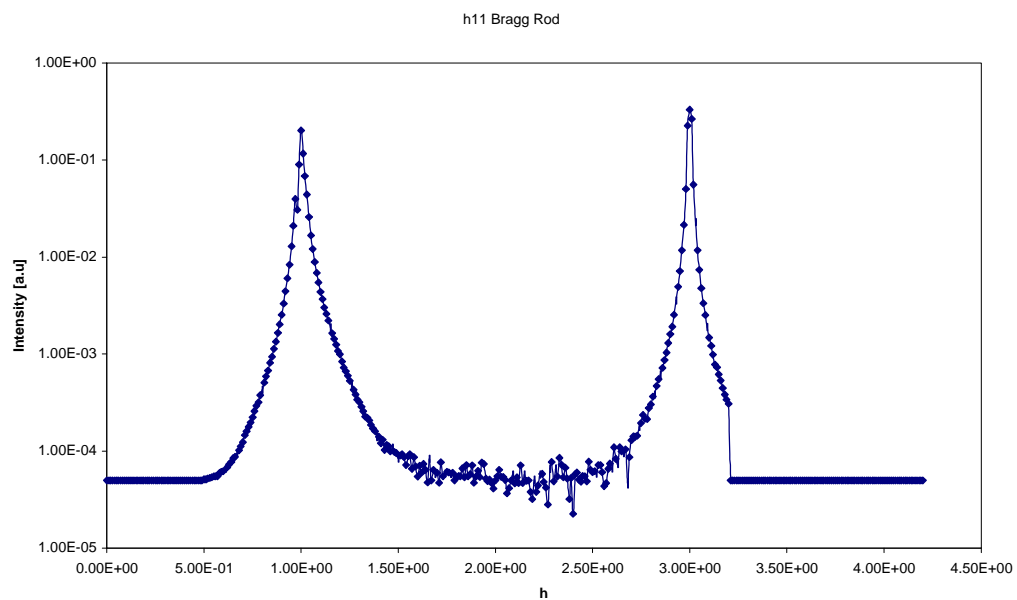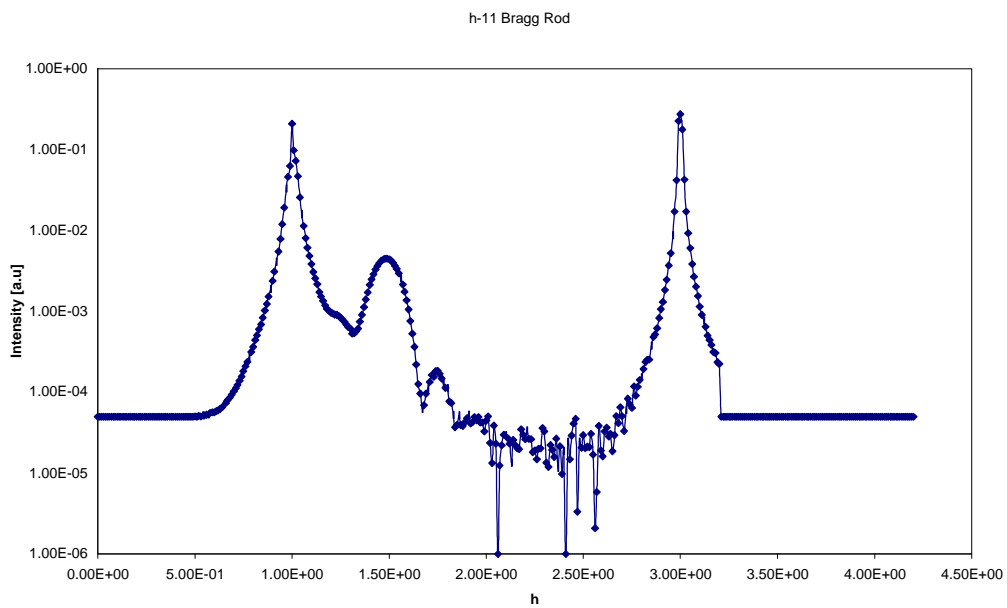
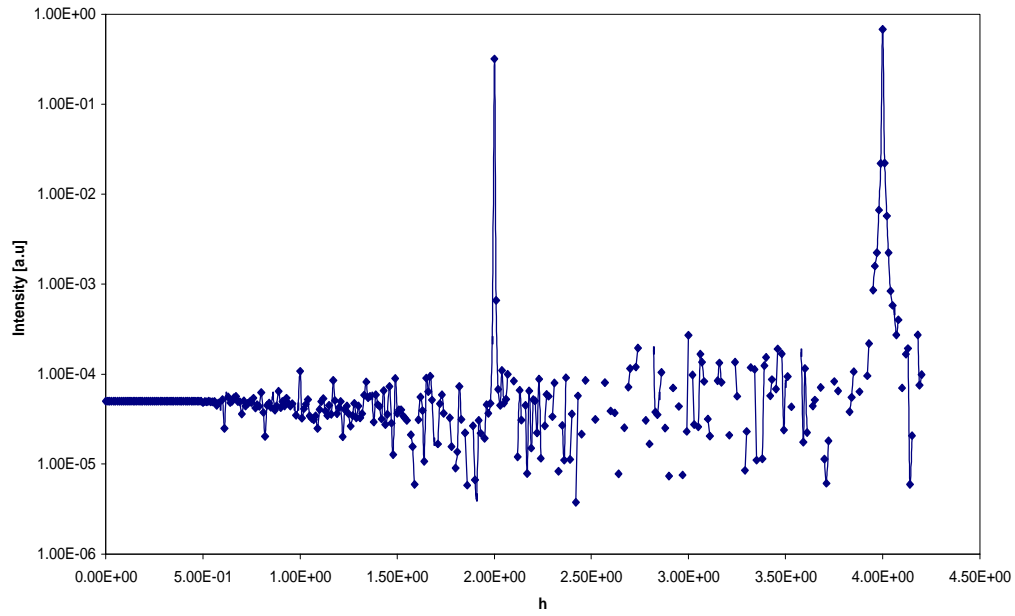h11 Bragg Rod
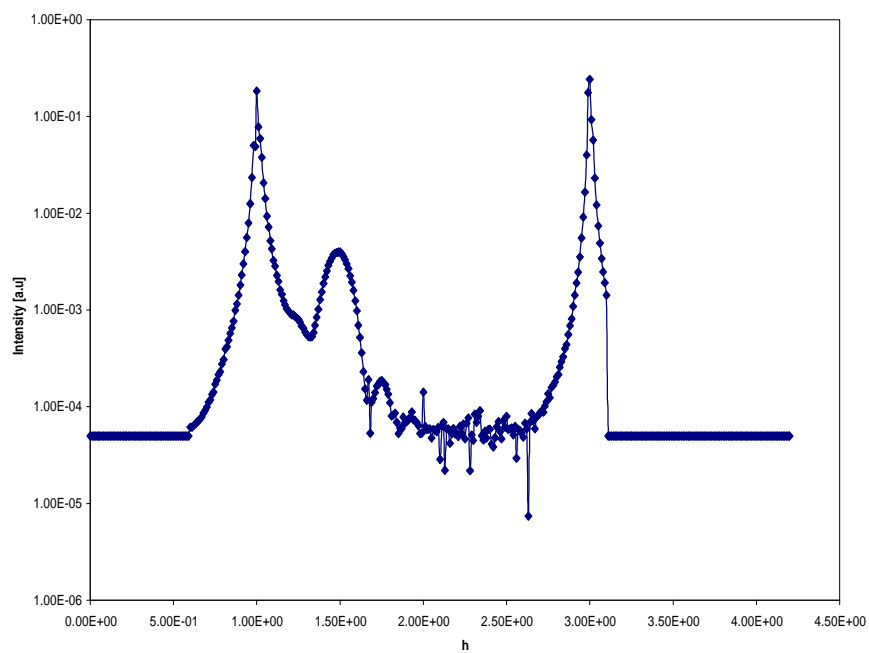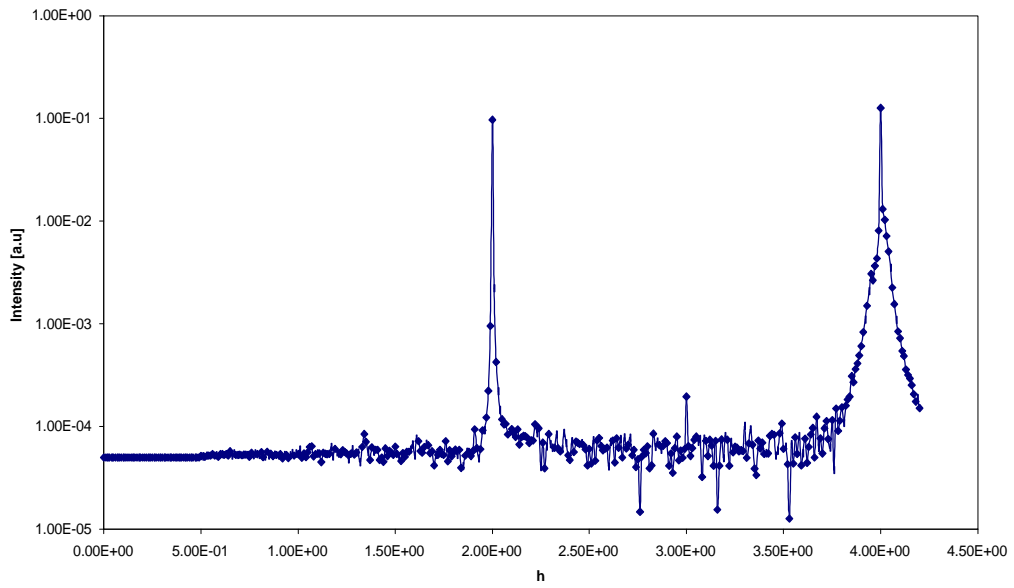
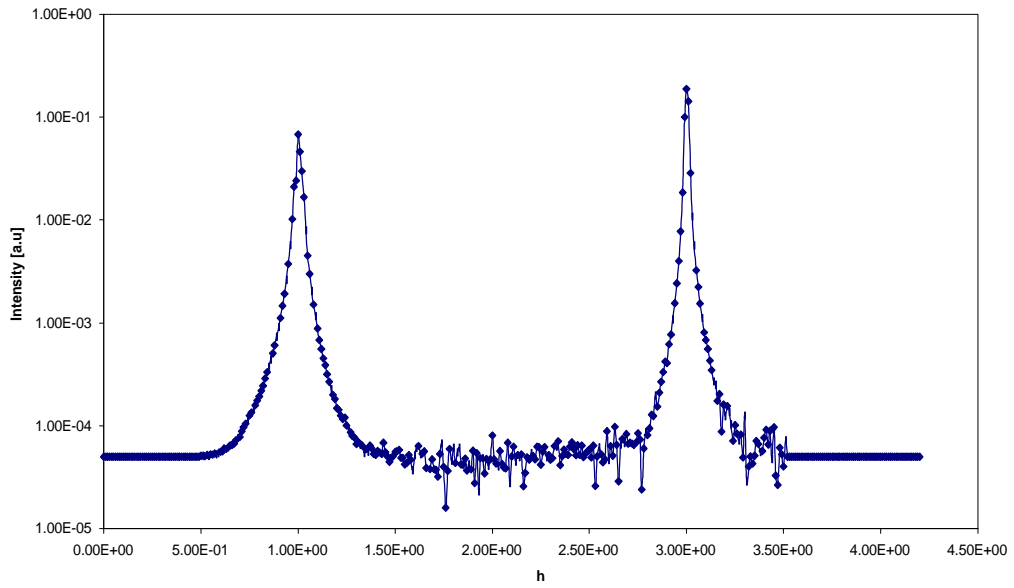h 1 -1 Bragg Rod

h 0 0 Bragg Rod

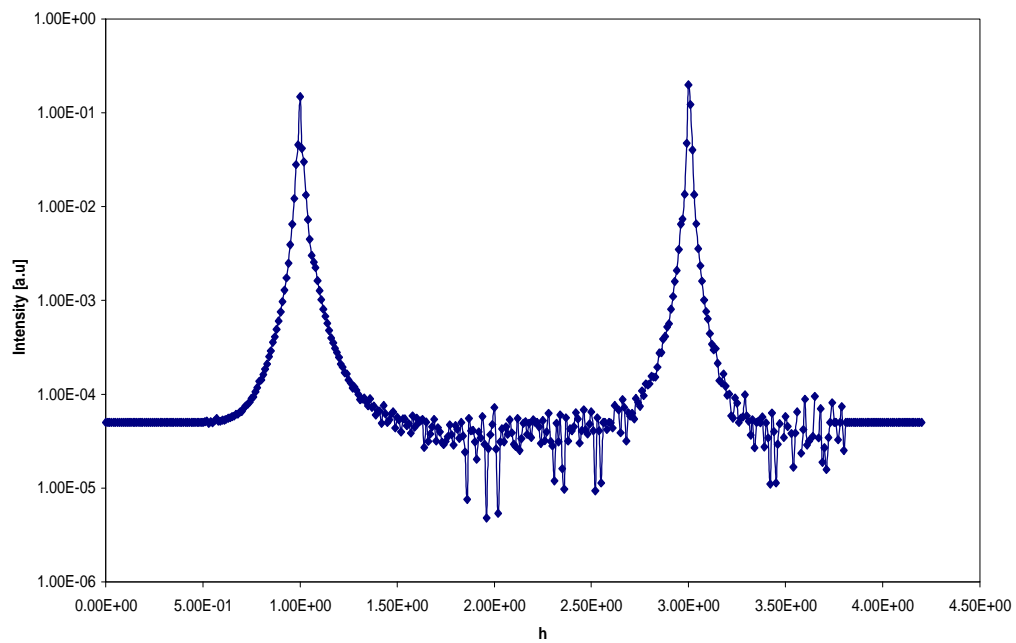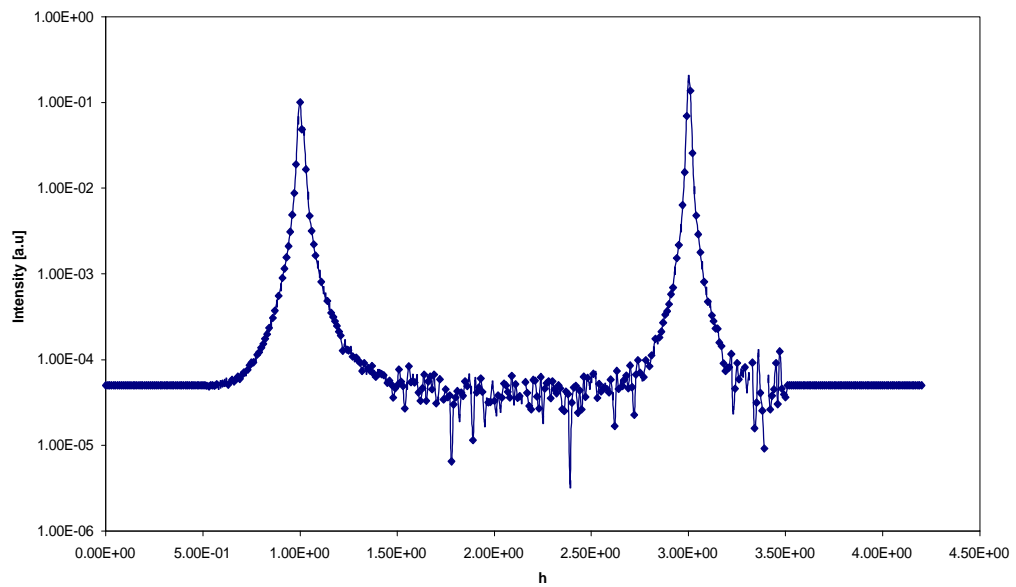h 0 -2 Bragg Rod
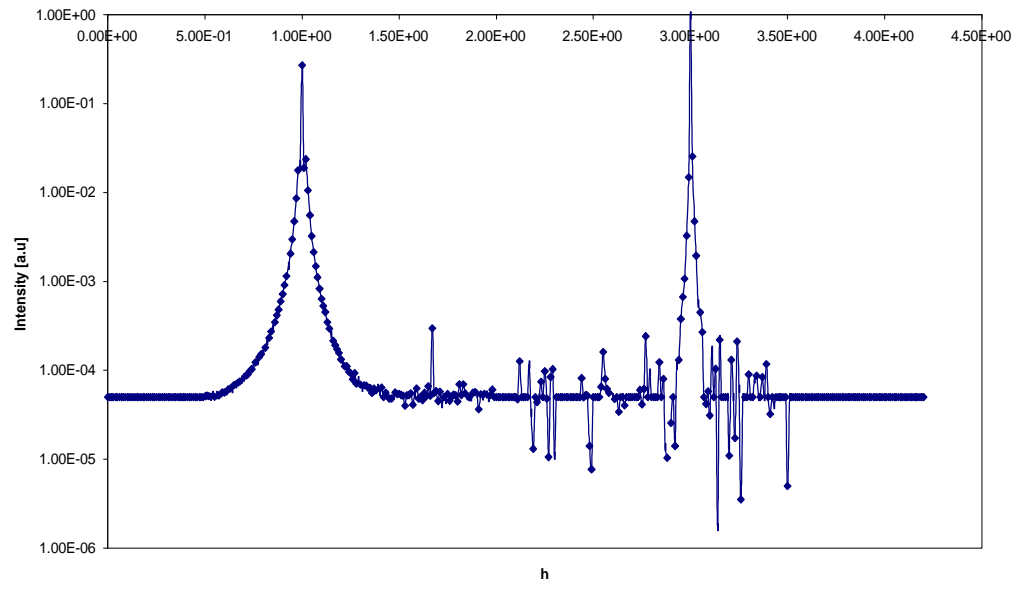
h 0 2 Bragg Rod

h 2 -2 Bragg Rod

h-2-2 Bragg Rod

h 3 1 Bragg Rod

h 3 -1 Bragg Rod

h 1-3 Bragg Rod

79

h-1-3 Bragg Rod

80

BIBLIOGRAPHY

1. P.R. Buseck, J.M. Cowley, and L. Eyring, Eds., High-Resolution Transmission Electron Microscopy and Associated Techniques (Oxford University Press, New York, 1988)

2. J.C.H. Spence, in: Experimental High Resolution Electron Microscopy (Oxford University Press, 1988, 2nd ed.).

3. W.J. de Ruijter and J.K. Weiss, Ultramicroscopy **50**, (1993) p. 269.

4. R. Sinclair, et al, Acta Crystallographica A **44,** 965 (1988).

5. P. Hirsch, et al, in: Electron Microscopy of Thin Crystals (Krieger, Malabar FLA, 1977).

6. S. Nakatani and T. Takahashi , Surf Sci **311** (1994) p.433.

7. S.R Andrews and R.A. Cowley, J. Phys. C **18** (1995) p.6427.

8. I.K. Robinson, Phys. Rev. B **33** (1986) p.3830.

9. T. Takahashi, S. Nakatani, T. Ishikawa and S. Kikuta, Surf. Sci. **191** (1987) L825.

10. R. Colella, Phys. Rev. B **43** (1991) p.13827.

11. D.G Stearns, J. Appl. Phys. **65** (1989) p.491.

12. D.G Stearns, J. Appl. Phys. **71** (1992) p.4286.

13. A.P. Payne and B.M Clemens, Phys. Rev. B **47** (1993) p.2289.

14. D.Brown, T.C.Q.Noakes, D.P.Woodruff, P.Bailey and Y.Le Goaziou, J.Phys.:Condens.Matter **11** (1999) p.1889.

15. P.Bailey, T.C.Q.Noakes and D.P.Woodruff, Surf.Sci.**426** (1999) p.358 .

16. D.Brown, P.D.Quinn, D.P.Woodruff, P.Bailey and T.C.Q.Noakes, Phys.Rev. B **61** (2000) p.7706.

17. D.Brown, D.P.Woodruff, T.C.Q.Noakes and P.Bailey, Surf.Sci **476** (2001) L241-L246.

18. D.E Sayers, E.A Stern and F. Lytle, Phys. Rev. Lett. **27** (1979) p.1204.

19. E.A Stern, Phys. Rev. B **10** (1974) p.3027.

20. J. Goulon, Physica B **158** (1989) p.5.

21. P.H . Citrin, Surf. Sci. **299** (1994) p.199.

22. P. Kizler, Phys. Lett A **172** (1992) p66.

23. M.Tegze, G.Faigel, Nature **380** (1996)p. 49.

24. T.Gog, P.M Len, G.Materlik, D.Bahr, C.S. Fadley,C.Sanchez-Hanke, Phys.Rev. Lett. **76** (1996) p.30.

25. T.Gog, R.Eisenhower, R.H.Menk, M.Tegze, Journal of Electron Spectroscopy, **92** (1998) p.123**.**

26. B.W. Batterman, Phys. Rev. **133** (1964) A759.

27. B.W. Batterman, Phys. Rev. Lett . **22** (1969) p.703.

28. J.A. Golovchenko, B.W. Batterman and W.L. Brown, Phys. Rev. B **10** (1974) p.4239.

29. S.K. Andersen, J.A. Golovchenko and G. Mair, Phys. Rev. Lett . **37** (1976) p.1141.

30. J.R. Patel, J. Zegenhagen, P. Freeland and D.M. Chen, J. Vac. Sci. Technol. B7 (1989) p.894.

31. R. Paniago, H. Homma, P. C. Chow, and S.C. Moss, Z. Barnea, S.S. P. Parkin and D.Cookson, Phys. Rev. B **52** (1995) p.52.

32. M. Suzuki and Y. Taga, Phys. Rev. B **52**, (1995) p.361.

33. S.K. Sinha, E. B. Sirota, S. Garoff and H.B Stanly, Phys. Rev. B **38**, (1988) p.2297.

34. Y.H. Phang, D. E. Savage, R. Karioties and M. G. Lagally, J. Appl. Phys. **74** (1993) p.3181.

35. R. E. Geer, R. Shashidhar, A. F. Thibodeaux and R.S. Duran, Phys. Rev.Lett. **71** (1991) p.1391.

36. Y. Yacoby, M. Sowwan, E. Stern, J. Cross, D. Brewe, R. Pindak, J. Pitney, E.B. Dufresne and R. Clark, nature materials (2002) p.99.

37. M. Sowwan, Y. Yacoby, J. Pitney, R. MacHarrie, M. Hong, J. Cross, D.A Walko, R. Clark, R. Pindak and E. Stern. Phys. Rev B. **66** (2002) 2053-2065.

38. Y. Yacoby, R. Pindak,R. MacHarrie, L. Pfeiffer, L. Berman and R. Clark, J. Phys.:Condens. Matter **12** (2000) p.3929.

39. Y. Yacoby, Solid State Comm. **91** (1994) p529.

40. H. Baltes ,Y. Yacoby, R. Pindak,R., L. Pfeiffer, L. Berman and R. Clark, Phys.Rev.Lett. **79** (1997) p1285.

41. M. Hong, J. Kwo, A.R. Kortan, J.P. Mannaerts and A. M. Sergent, Science **283** (1999) p.1897.

42. A.R. Kortan, M. Hong, J. Kwo and J.P. Mannaerts, Phys. Rev. B **60** (1999) p.10913.

43. I. Takahashi, S. Takayoshi and J. Harada, J. Phys.:Condens. Matter **5** (1993) p.6525.

44. T. Shimura, H. Misaki, M. Umeno, I. Takahashi and J. Harada, J. of Crystal Growth **166** (1996) p.786.

45. M. Hong, M. Passlack, J.P. Mannaerts, J. Kwo, S.N.G. Chu, N. Moriya, S.Y. Hou and V.J. Fratello, J. Vac. Sci. Technol. B **14**, (1996) p2297.

46. M. Hong, M.A. Marcus, J. Kwo, J.P. Mannaerts , A. M. Sergent, L.J. Chou, K. C. Hsieh and K.Y. Cheng, J. Vac. Sci. Technol. B **16**(3) (1993) p.1395.